Sedimentary Geology 480 (2025) 106854

Contents lists available at ScienceDirect

Sedimentary Geology

journal homepage: www.elsevier.com/locate/sedgeo

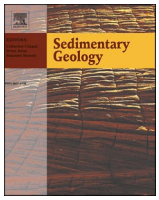

Origin and deposition of deepwater homogenites from a sedimentological perspective: Examples from offshore SW Taiwan

Radha Krishna Pillutla [a,b], Andrew Tien-Shun Lin [a,b,c,*], Jen-Chu Yeh [b], Gueorgui Ratzov [d], Nathalie Babonneau [e], Shu-Kun Hsu [a,b], Chih-Chieh Su [a,f], Serge Lallemand [g], Ludvig Löwemark [a,h]

[a] Earth System Science, Taiwan International Graduate Program, Academia Sinica and National Central University, Taiwan
[b] Department of Earth Sciences, National Central University, Taiwan
[c] Carbon Storage and Geothermal Research Center, National Central University, Taiwan
[d] Université Côte d'Azur, CNRS, Observatoire de la Côte d'Azur, IRD, Géoazur, Nice, France
[e] Geo-Ocean, UMR 6538, Univ. Brest, CNRS, Ifremer, F-29280, Plouzané, France
[f] Institute of Oceanography, National Taiwan University, Taiwan
[g] Géosciences Montpellier, Montpellier University, CNRS, France
[h] Department of Geosciences, National Taiwan University, Taiwan

ARTICLE INFO

Editor: Dr. Massimo Moretti

Keywords:
Silty turbidite-homogenites
Lithofacies
Depositional processes
Grain-size analysis

ABSTRACT

A giant piston core, MD18–3548 (20.07 m) was collected from a perched basin in the Taiwan accretionary wedge, at a water depth of 1752 m. Detailed grain-size analysis, ^{14}C accelerator mass spectrometry (AMS) dating, and computed tomography (X-CT) scans of the core were performed. Four types of lithofacies, namely hemipelagic sediments, silty turbidite-homogenites, turbidites, and thin silty layers, are identified, along with seventeen event beds. A total of fourteen ^{14}C AMS dating were carried out, with the depositional ages of the event beds being calculated based on the sedimentation rate of hemipelagites. The oldest event bed is ~12 cal kyrs BP, while the youngest event bed is ~64 cal yrs BP. All seven homogenite units are floored by a thin (usually <10 cm thick), coarsening-upward first and then fining-upward unit, capped by a thick structureless mud totally devoid of bioturbation. The average thickness of homogenite units is ~150 cm, while the thickest homogenite unit is ~200 cm. These homogenite units can be compared to similar deposits reported elsewhere and find particularly that these units exhibit a basal layer with gradual coarsening and fining upward trend in grain size. We therefore propose a new depositional model for the silty turbidite-homogenite units in seismically-shaken enclosed basins. This model takes into account the coarsening-then-fining upward deposition of the basal layers, reported for the first time.

1. Introduction

The island of Taiwan is widely recognized for having one of the highest sediment yields globally, owing to its steep slopes, frequent earthquakes, and typhoons which drive rapid mass-wasting (Dadson et al., 2003; Li et al., 2012). Submarine basins in seismically active regions often preserve sedimentary records initiated by mass wasting processes and gravity-driven flows (McHugh et al., 2011). Following the identification of the fine-grained homogenite caused by a Mediterranean tsunami (Kastens and Cita, 1981; Cita et al., 1996), there have been reports of similar uniform layers in other enclosed marine basins. Earlier reports described similar deposits as 'unifites' (Stanley, 1981), 'mega-turbidites' (Cita et al., 1984; Rebesco et al., 2000), and mega-deposits (San Pedro et al., 2017). These event deposits have been linked to the effects of subaqueous earthquakes or volcanic eruptions (Chapron et al., 1999; Beck et al., 2007; Bertrand et al., 2008; Carrillo et al., 2008; Çağatay et al., 2012). The term 'homogenite' refers to the structureless fine-grained beds, that are homogenous in nature (Polonia et al., 2013). Earthquake shaking or tsunami waves may remobilize/resuspend shelf/slope sediments, resulting in deposition of homogenites by gravity-flow processes (McHugh et al., 2016; Ikehara et al., 2021; Schwestermann et al., 2021; Usami et al., 2018; Cita et al., 1984, Kastens and Cita, 1981).

* Corresponding author at: Department of Earth Sciences, National Central University, Taiwan.
E-mail address: andrewl@ncu.edu.tw (A.T.-S. Lin).

https://doi.org/10.1016/j.sedgeo.2025.106854
Received 24 December 2024; Received in revised form 24 February 2025; Accepted 28 February 2025
Available online 2 March 2025

Nevertheless, gravity flows triggered in a similar manner also play a role in the formation of turbidites (Middleton, 1993). Therefore, it is imperative to distinguish between turbidites and homogenites, as demonstrated in this study. The descriptive term 'homogenite' is used to describe the uniform nature of the beds, particularly in relation to their mud component (Shiki and Cita, 2008). Most researchers (Beck et al., 2007; Çağatay et al., 2012; McHugh et al., 2016) classify these deposits as turbidite-homogenite sequences, which fundamentally comprise two components: a coarse basal section, overlain by the homogenite layer. The homogenite layer is the upper part of turbidite-homogenite unit. However, the base of these homogenites are usually coarser than the mud component, and are generally described as a normal-graded erosive surface, with laminations (Cita et al., 1984; St-Onge et al., 2012). These homogenites, which are characterized by significant thickness, are identified in acoustic sub-bottom profiles as transparent units and are deposited in deep perched or semi-enclosed basins. Deepwater turbidites are found in other areas such as in the Japan Trench system (Kanamatsu et al., 2023; Ikehara et al., 2016; Strasser et al., 2024), Gulf of Corinth (Beck et al., 2007), Hedberg Basin (Tripsanas et al., 2004), and the Marmara Sea (McHugh et al., 2006) and they are all interpreted as deposits triggered by earthquakes.

However, there are still some inconsistencies between the depositional models for the reported deepwater homogenites. In this study, we present new results obtained from a semi-enclosed basin in offshore SW Taiwan. We identify and report thick homogenites ranging from 1 to 2 m in thickness, for the first time from offshore southwestern Taiwan. The main objectives of this study are as follows: (a) provide detailed sedimentary facies descriptions, with a particular focus on homogenites; (b) differentiate between homogenites and other event beds; and (c) discuss the depositional model for the homogenites.

2. Geological setting and sampling and analytical methodology

2.1. Geological setting

In Taiwan, the convergence of two plates, namely the Eurasian plate and the Philippine Sea plate, generates abundant and frequent seismicity, which poses a substantial seismic risk to human settlements (Hutchings and Mooney, 2024). Subduction of the Eurasian Plate (South China Sea, SCS) underneath the Philippine Sea Plate at the Manila Subduction Zone (MSZ) initiated during the Early Miocene (22–25 Ma) and continued to the present day (Fuller et al., 1983; Bellon and Yumul, 2000; Yumul et al., 2003; Queano et al., 2007). The Philippine Sea Plate moves northwest and overrides the Eurasian Plate at a rate of 7–8 cm/yr (Ranken et al., 1984; Seno et al., 1993; Yu et al., 1999; Yu and Kuo, 2001).

The island of Taiwan experiences roughly four typhoons per year with nominal annual precipitation of 2500 mm/yr, resulting in rapid mass-wasting processes (Dadson et al., 2003; Huang et al., 2016). Between 1970 and 1999, Taiwan supplies 384 Mt. yr^{-1} of suspended sediment to the ocean, representing 1.9 % of estimated global suspended sediment discharge (Milliman and Syvitski, 1992). Submarine canyons like the Gaoping Canyon, Penghu Canyon, Formosa Canyon, and Fangliao Canyon act as channels for delivery of continental sediments to the deep-sea (Fig. 1).

The deformation front (DF) is the separation between two distinctive tectonic provinces, the SCS continental margin on the west and the Taiwan subduction complex on the east. (Lin et al., 2008). The DF extends from the northern end of the Manila Trench to the Tainan area onshore Taiwan (Liu et al., 2004; Fig. 1). To the east of the DF, an accretionary wedge with a series of N-S trending parallel folds and thrusts, has been formed by the plate convergence (Liu et al., 1997; Lin et al., 2008; Huang et al., 2021). The lower slope area of the accretionary wedge offshore SW Taiwan consists of a series of ridges. The seismicity offshore SW Taiwan concentrates within the slab (e.g., intra-slab subduction earthquakes) and not in the accretionary wedge (Lin et al., 2009), which is considered to be a zone of tectonic escape (Lacombe et al., 2001), and is therefore identified as a zone of reduced seismic activity in Taiwan, as compared to other zones where significant collisional processes are ongoing (Chen et al., 2008). Most of the intra-slab subduction earthquake events lie in ~30–60 km depth range with some events extending to a maximum depth of about 80 km. The best examples of intra-slab subduction earthquake in this region are the 2006 Pingtung doublet quake, located at depth range of ~44–50 km (Lin et al., 2009). Lin et al. (2009) pointed out that the splay fault and plate boundary megathrust offshore SW Taiwan are similar to those found in the Nankai Trough (Park et al., 2002; Moore et al., 2007), and pose great seismic and tsunami threat, endangering the population of Taiwan and its neighboring regions.

The historical records for this area are limited, with the sole documented earthquake being the one that occurred on February 15, 1661 (near Tainan, magnitude of 7.1, Ng et al. (2009)) which is associated with the Penghu tsunami (Yu et al., 2023). Additionally, several historical records point to a disastrous tsunami (unknown trigger) on the southwestern coast of Taiwan around 1781 to 1782, with a reported death toll of >40,000 (Li et al., 2015).

2.2. Methods, sampling and analytical methodology

A giant piston core, MD18–3548 (Latitude: 21°52.73′N, Longitude: 119°57.17′E), was collected onboard R/V *Marion Dufresne II* (5–27 June 2018) during the MD214 EAGER (Extreme events Archived in GEological Records) cruise. The core was retrieved from a semi-enclosed basin (Figs. 1, 2) offshore southwestern Taiwan, with the purpose of studying event beds like seismoturbidites and homogenites. The perched/semi-enclosed basin features a bathymetric depression of approximately 100 m in height with two small outlets (Fig. 2). This basin is connected to a shallower, elongated slope basin to the north. The perched basin setting was specifically chosen to study event beds because of its location. Positioned far from both Gaoping Canyon and Penghu Canyon, our perched basin is devoid of terrestrial sediment input. Consequently, this isolation enables the exclusion of influences such as typhoons, severe rainfall, and other similar events that would typically be recorded in sediment cores retrieved from canyons. High-resolution CHIRP profiles serve as exceptional tools for identifying homogenites, given their acoustically transparent and massive nature (McHugh et al., 2020; Cattaneo et al., 2020; Cita, 2008; Strasser et al., 2024). A CHIRP profile, along with cross-sections trending SW-NE and NW-SE, was acquired for MD18–3548, with the red line indicating the depth of core penetration (Fig. 3A, B, C). Sediments pertaining from enclosed/semi-enclosed basins are remarkable for studying these types of event beds. The small semi-enclosed basin has a width of ~8 km and has a slope of <12° from basin edge to basin floor. MD18–3548 is 20.07 m long and was obtained from a depth of 1752 m below sea level. The core was split onboard into archive and working halves. Detailed core-description were visually performed to make note of various sedimentary features, such as changes in grain size, grain-size breaks, and colour changes, etc. Non-destructive analysis included photographing the cores, along with measurements of physical parameters (i.e., P-wave velocity, gamma density, magnetic susceptibility, porosity, and colorimeter) using a Geotek Multi-Sensor Core Logger (MSCL).

Selected depths were chosen for foraminifera dating based on foraminifer abundance. Additionally, X-ray Computed Tomography (X-CT) scan was performed on all the sections, and the core was then sampled using a U-channel, to facilitate grain size analysis. From the U-channel, samples were collected at intervals of 5 cm in the case of hemipelagites and homogenites, and at intervals of 1 cm in the case of event beds (i.e., thin silt layers, turbidites, and silty turbidite layer at the base of the homogenites, see Section 3.1 for lithofacies), across the entire length of the core. Chemical pre-treatment for grain size was performed using 15 % hydrogen peroxide and 10 % hydrochloric acid over a period of 2–4 days. This process effectively removes sea salt, organic matter, and

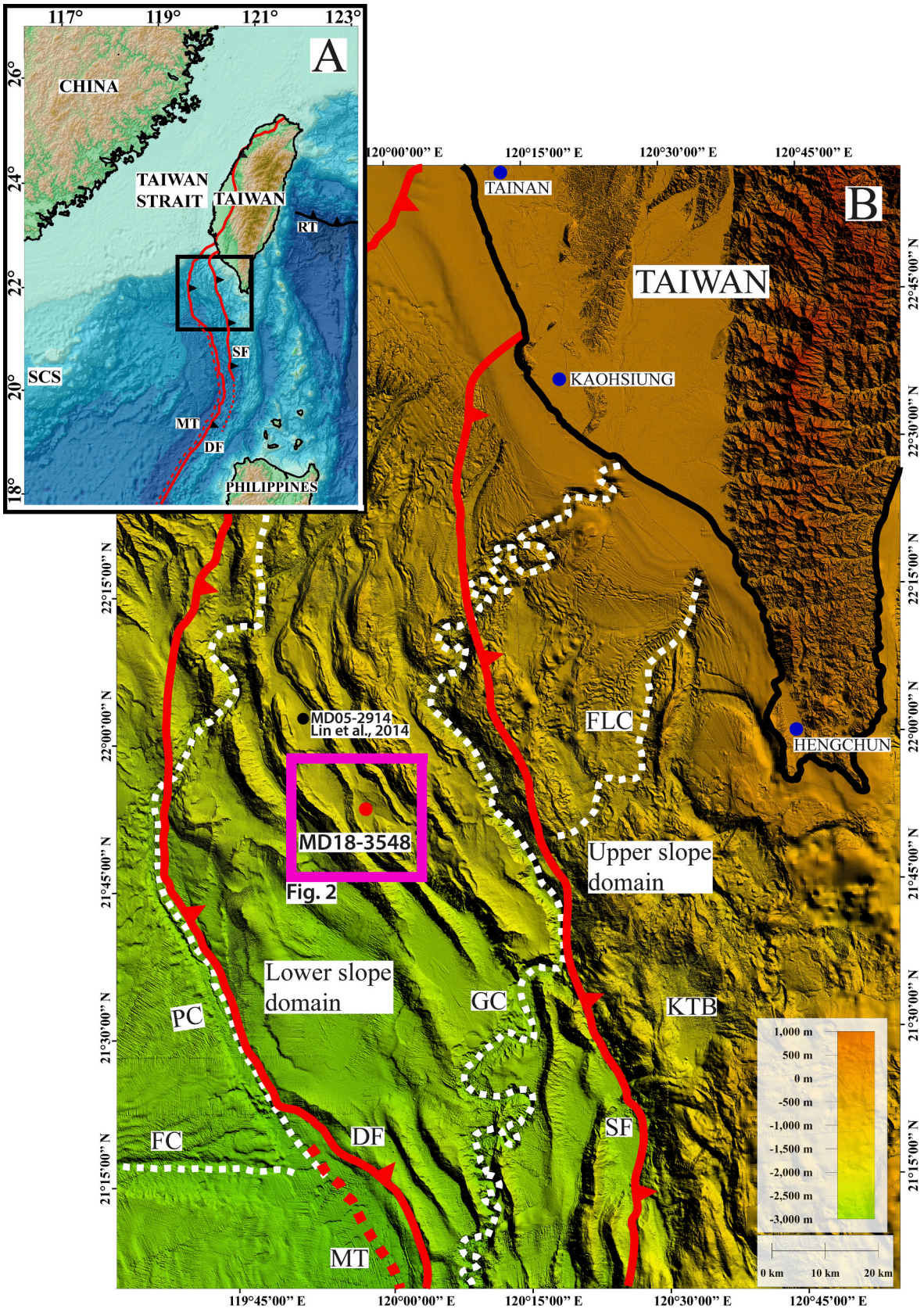

Fig. 1. (A) Map of Taiwan, along with the deformation front, splay fault, and Manila Trench. (B) Inset (black rectangle, Fig. 1A) displays the regional tectonic elements. The purple rectangle in offshore SW Taiwan marks the study area, with a red dot showing the core location. Black dot northwest of study area shows the core location of MD05–2914 (Lin et al., 2014). White, dotted lines show the course of submarine canyons, and red thick lines indicate the deformation front and splay fault. Blue filled circles represent major cities. Abbreviations: DF- Deformation Front; FC- Formosa Canyon; FLC- Fangliao Canyon; GC- Gaoping Canyon; KTB- Kenting Basin; MT- Manila Trench; PC- Penghu Canyon; RT- Ryukyu Trench; SCS- South China Sea; SF- Splay Fault.

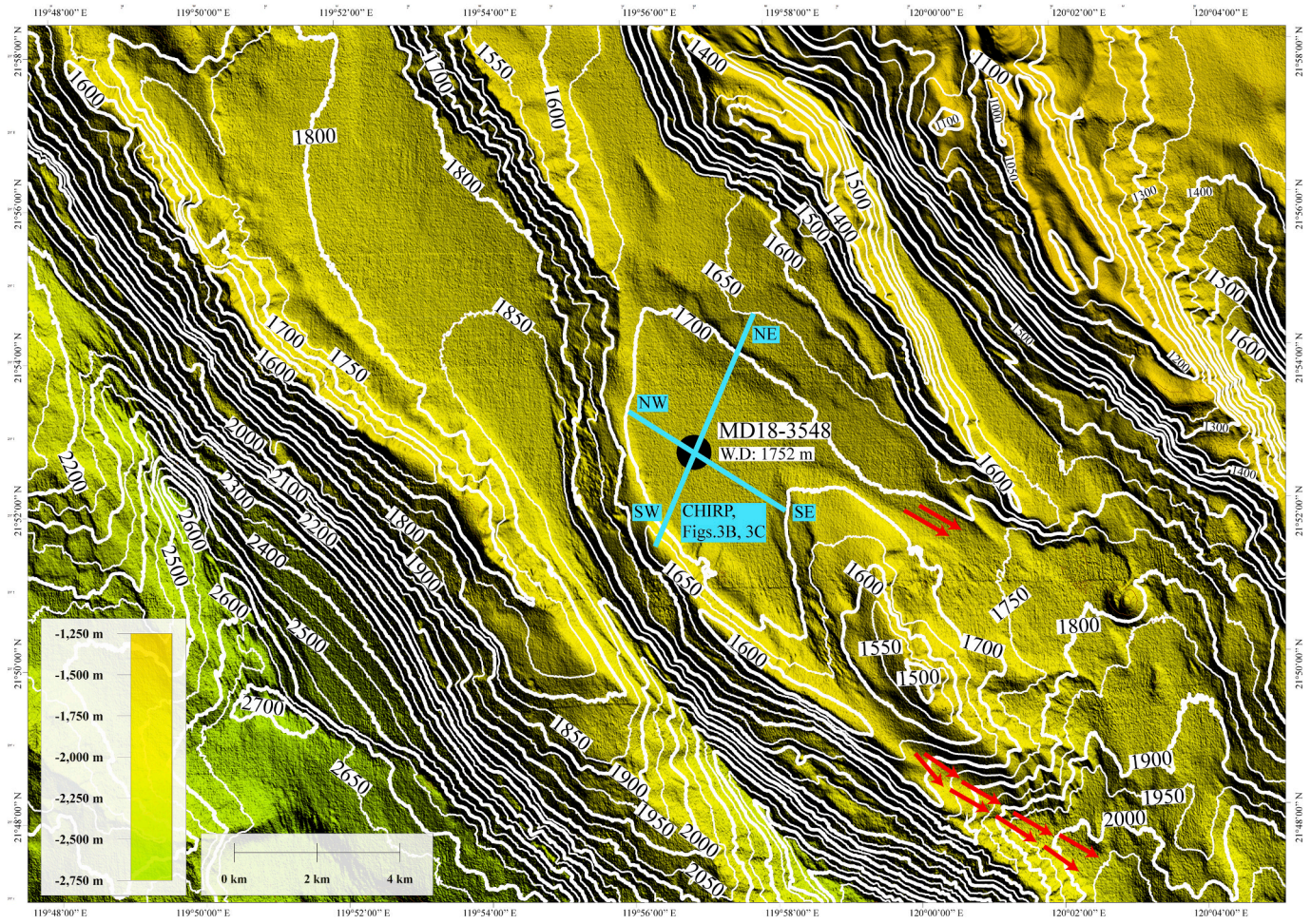

Fig. 2. Bathymetric map showing the core location MD18–3548, in a semi-enclosed basin (black dot), along with the depth contours. The thick white line indicates the 100 m gap of depth contour, whereas the thin white line indicates the 50 m gap in depth contour. Cyan-colored lines indicate the SW-NE, NW-SE, and CHIRP profile (sub-bottom profiler). Red arrows mark the two small outlets of the semi-enclosed basin.

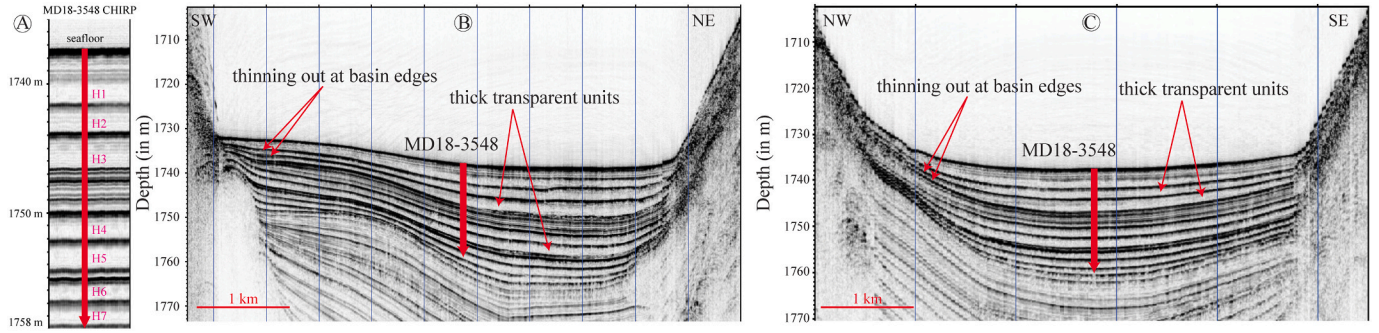

Fig. 3. (A) MD18–3548 CHIRP profile. (B, C) SW-NE and NW-SE trending CHIRP section traversing across MD18–3548 site, showing thick transparent layers and thinning out at basin edges. The thick red line in (A), (B), and (C) represent the depth of core penetration. Also marked are the homogenite units identified in the core (H1 to H7).

carbonate content. Subsequently, the samples underwent deflocculation in an ultrasonic device and then later using a solution of sodium hexametaphosphate before proceeding to the final analysis. The grain-size analyses were conducted at the Sediment Analysis Lab of National Central University (SALNCU), using a laser particle analyzer, the Beckman Coulter LS 13320 was employed, for grainsize range from 0.020 μm to 2000 μm. Additionally, specific depths were selected for examination under the optical microscope and smear slides were prepared for analysis.

In total, 548 samples were analyzed. The resulting raw data was brought into an excel program GRADISTAT (Blott and Pye, 2001). Statistical equations enable us to obtain grain size parameters like mean, sorting, skewness and kurtosis. These statistical formulae (Geometric method of moments, with metric units) are derived from the GRADISTAT program (Blott and Pye, 2001), which was originally adapted from Krumbein (1938) and Folk and Ward (1957). Subsequent to the completion of detailed grain-size analysis, inspection of X-CT images, and core photographs, the identification and delineation of lithofacies

boundaries were conducted (Fig. 4), with the identifying criteria outlined in Table 4. Furthermore, the density and magnetic susceptibility plots do not significantly help in demarcating the lithofacies (e.g., supplementary fig. 4).

Foraminifera (planktonic) were picked from various depths, including hemipelagic sediments, and the basal layer of homogenites. A total of fourteen AMS radiocarbon dating were obtained from MD18–3548, of which thirteen were from foraminifera and one from a Scaphopoda tusk shell (Table. 1). The tusk shell was found in the event bed and was intact. The shell was carefully cleaned using distilled water and further sonicated to remove any debris. All the thirteen foraminifers picked were >125 μm size fraction. Further processing of the foraminifers was done by washing them carefully in distilled water and then adding sodium hypochlorite solution. The solution was left to stand overnight, followed by another round of washing with distilled water. This process aimed to remove any debris that might have been present inside the foraminifer shells but went unnoticed during the initial picking. There is a usual difference of 2–3 mg before and after the processing steps. For each date, approximately 5–10 mg of planktonic foraminifera (including species such as *Globigerinoides ruber*, *Globigerinoides conglobatus, Orbulina universa* and *Trilobatus sacculifer*) were selected, and 12.8 mg was used for the tusk shell. The ^{14}C dating process involved two sets of Accelerator Mass Spectroscopy measurements. Specifically: A) National Taiwan University (Taiwan), utilized an HVE 1.0 MV Tandetron model 4110 BO for 'nine' of the samples; B) Beta Analytic Laboratory (USA) employed NEC AMS for analysis with 'five' samples sent for testing.

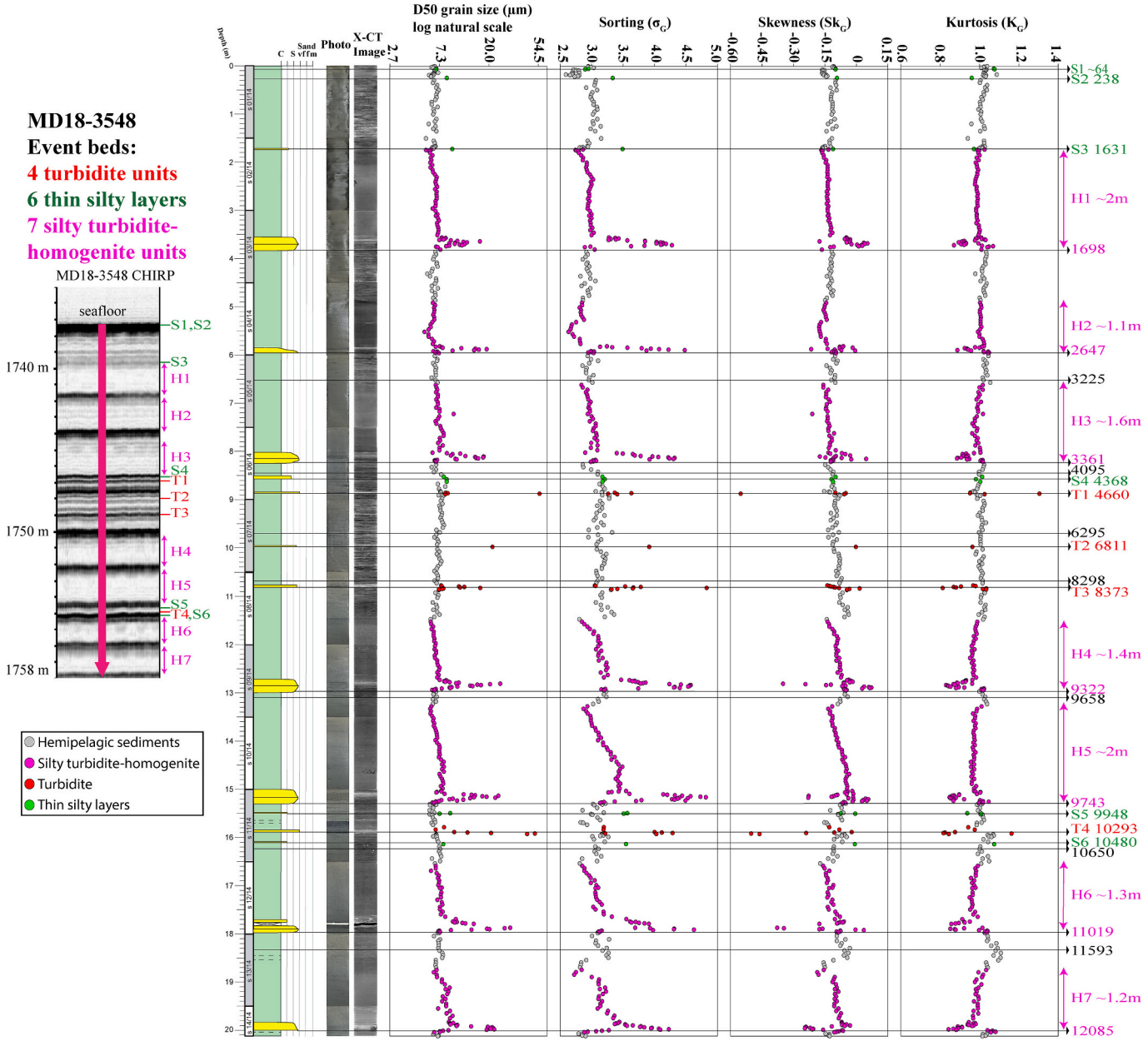

Fig. 4. Lithological description, core photography, X-CT images, and grain size statistics (D50, sorting, skewness, and kurtosis) for the core MD18–3548. Filled gray, red, green, and pink circles represent hemipelagites, turbidites, thin silty layers, and silty turbidite-homogenite units respectively. Black text represents calibrated ^{14}C ages, in cal BP years. Pink, red and green text represent emplacement ages of silty turbidite-homogenites, turbidite and thin silty layers. CHIRP image of the core is shown on the left, along with the event beds marked. D50 uses log natural scale.

Table 1
^{14}C AMS dating from foraminifers of MD18–3548. BP calibrated ages are obtained using Calib 8.2 software from Stuiver and Reimer (1993). Calibrations show 2σ median probability age with lower and upper range. 1: Sample sent to NTUAMS, 2: Sample sent to Beta-Analytics, 3: Sample is a tusk shell (Scaphopoda).

Depth in core (cm)	Depth in background sediments (cm)	^{14}C yr BP with error	2 σ cal BP median probability, lower and upper age range, ΔR = 0	Notes
371–374[1]	Event bed	3104 ± 70	2736, 2497–2946	Silty turbidite basal layer
372–376[2,3]	Event bed	3540 ± 30	3266, 3103–3410	Silty turbidite basal layer
652–655[1]	337–340	3507 ± 51	3225, 3025–3398	
802–804[2]	Event bed	4650 ± 30	4687, 4517–4834	Silty turbidite basal layer
843–846[2]	369–372	4200 ± 30	4095, 3915–4275	
967–970[1]	482–485	6064 ± 56	6295, 6112–6477	
1065–1068[1]	580–583	8007 ± 68	8298, 8103–8501	
1288–1292[2]	Event bed	9660 ± 30	10,382, 10,225–10,550	Silty turbidite basal layer
1310–1319[2]	689–692	9130 ± 30	9658, 9515–9864	
1519–1522[1]	Event bed	10,261 ± 79	11,232, 10,992–11,555	Silty turbidite basal layer
1625–1628[1]	795–798	9846 ± 71	10,650, 10,393–10,987	
1787–1790[1]	Event bed	12,708 ± 96	14,226, 13,859–14,663	Silty turbidite basal layer
1831–1834[1]	864–867	10,520 ± 66	11,593, 11,307–11,865	
1994–1997[1]	Event bed	11,085 ± 82	12,448, 12,150–12,673	Silty turbidite basal layer

3. Results and interpretations

3.1. Lithofacies

Core MD18–3548 is primarily composed of silt-sized material. Four lithofacies have been identified, namely: (a) hemipelagic sediments, (b) silty turbidite-homogenite units, (c) turbidites, and (d) thin silty layers. Apart from hemipelagic sediments, the other three facies are categorized as event deposits.

3.1.1. Hemipelagic sediments

Description: Hemipelagic sediments are primarily composed of silt and are light greyish in colour. They constitute ~45 % of the entire length of the core. Their grain-size D50 values range from 5.61 μm (very fine silt) to 8.29 μm (fine silt), with an average of 7.79 μm (very fine silt). These sediments are predominantly fine-grained, with a relatively wider range of vertical grain size variations (Fig. 5a) compared to that of homogenites. They exhibit unimodal and bimodal grain-size distributions (Fig. 5e). The grain size characteristics of these sediments indicate poor sorting, fine skewed and mesokurtic nature. Various trace fossils, such as *Zoophycos*, *Chondrites*, *Phycosiphon*, *Thalassinoides*, are identified from X-CT images (e.g., supplementary figs. 1, 2, 3). Scattered foraminifera (largely well-preserved) are present throughout most of the hemipelagic sediments, with the exception of the top 6 m of the core, where forams were extremely sparse. Many of the hemipelagic sediments found at depths below approximately nine meters exhibit dark colored spots (mottling) or bandings, as seen in both the core photographs and the X-CT images (e.g., supplementary figs. 1, 2, 3).

Interpretation: The nature of fine grain size, moderate bioturbation, and no tractional sedimentary features of the hemipelagites indicate that the process of deposition is through slow suspension settling during quiet periods. However, thin mud/silt event layers can be bioturbated to resemble hemipelagic sediments. The relict lamina (e.g., broken parallel lamination) may serve as a distinguishing feature for recognizing thin and bioturbated mud/silt event layers. As these layers are scarce and inconclusive in their origin, we consider those layers as hemipelagites.

The dark colored spots or bandings seen in many sections of the core are interpreted to be iron sulfides. Similar occurrences of iron sulfides are seen from nearby cores (Huang et al., 2021), where sulfate-methane interface is located at a shallow depth of 5–10 m below seafloor (mbsf) (Chuang et al., 2013).

3.1.2. Silty turbidite-homogenite unit

Description: A total of seven 'silty turbidite-homogenite' units (H1 to H7) are identified from core MD18–3548 (Fig. 4), ranging in thickness from approximately 100 cm to 200 cm, with an average thickness of approximately 150 cm. For core MD18–3548, approximately 54 % of core length pertains to silty turbidite-homogenite units. All seven layers (H1 to H7) are floored by a thin silty layer, often <10 cm thick, and overlain by a thick, homogeneous unit. The thin silty layer at the base is called the 'silty turbidite' (basal layer) and the thick homogenous unit is referred to as 'homogenite' (upper layer). Together, both layers comprise a 'silty turbidite-homogenite' unit.

The grain size for the basal layer demonstrates a characteristic coarsening upward trend, followed by a fining upward trend (Fig. 6). The basal layer shows a gradational basal contact for some units (H1, H3, H4, H5, H6), and a sharp contact for other units (H2 and H7). Similarly, a gradational contact is observed between the basal layer and the upper layer. The D50 value for the basal layer ranges from 6.40 μm to 30.85 μm, spanning from very fine silt to medium silt. They exhibit unimodal, bimodal, and trimodal grain-size distributions (Fig. 5e). The X-CT scan images of the basal layer reveal minimal bioturbation (e.g. planolites-like burrows shown in H6 and H7 of Fig. 6) and presence of parallel laminations. All the basal layers are enriched in foraminifera, except for the H2 unit, which is nearly devoid of foraminifera, and the H3 unit, which has a lower concentration compared to other units. The concentration of foraminfera is highest at the basal part and shows a moderate decrease to near absence at the top part of the basal layer. Little to negligible quantities of broken foraminifera were observed in the basal layer of the homogenite. The base of the basal layer of the homogenite is identified by the characteristic change in X-CT images, marked by the sudden change from the underlying bioturbated sediments to parallel laminated silts (e.g., supplementary figs. 1, 2, 3).

The thick upper layer is massive and structureless, ranging from ~1 m to a maximum thickness of ~1.8 m. All seven upper layers exhibit a slight reduction in grain size, indicating a fining upward trend (normal grading). The X-CT images, combined with sorting statistics, are utilized to distinguish the boundaries between the overlying hemipelagic sediments and the underlying homogenites (Table. 4). An abrupt change in sorting, which is more pronounced, and skewness is observed in all upper layers, with the exception of the H2 layer (Fig. 4). The D50 value ranges from 5.44 μm (very fine silt) to 9.82 μm (fine silt), with an average of 7.37 μm (very fine silt). The entire homogenous layer also exhibits unimodal grain-size distribution (Fig. 5e). Sorting, skewness, and kurtosis show a sudden change at the boundary between the thick upper layer and the overlying hemipelagites. Both hemipelagites and homogenites are poorly sorted, with hemipelagites inclining towards the extremely poorly sorted category. X-CT images reveal structureless mud essentially devoid of bioturbation (Fig. 5b), aiding in differentiating the homogenites from the overlying hemipelagic sediments. Moreover, all the seven layers (H1 to H7) exhibit variations in magnetic susceptibility, displaying both decreases and increases within the unit, with no

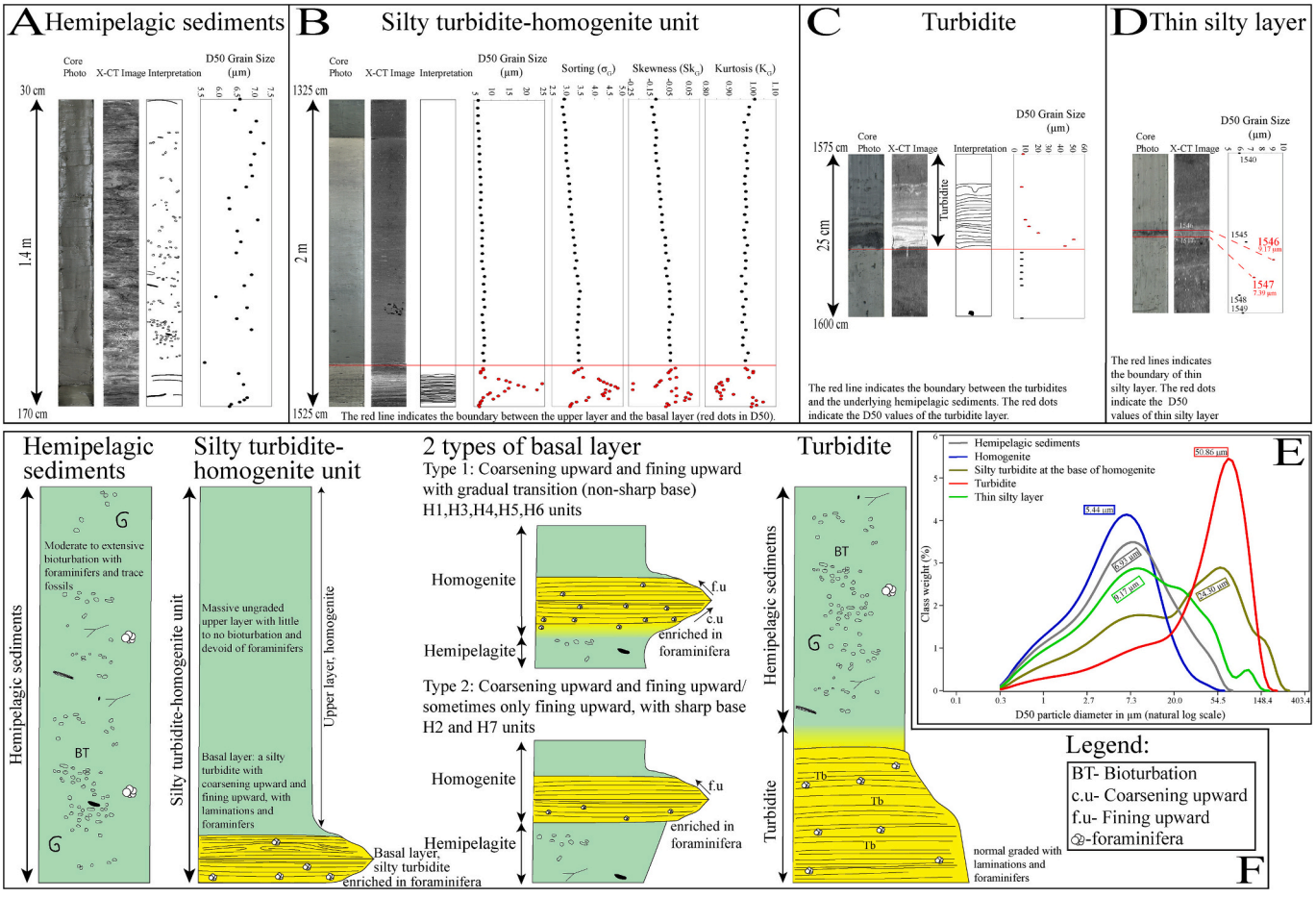

Fig. 5. Major lithofacies identified from MD18–3548. A- Hemipelagic sediments: background sediments; B, C, D- Event sediments; F- Visual representation of the lithofacies, along with the types of basal layer; *E*- D50 particle size vs cumulative wt% of the lithofacies.

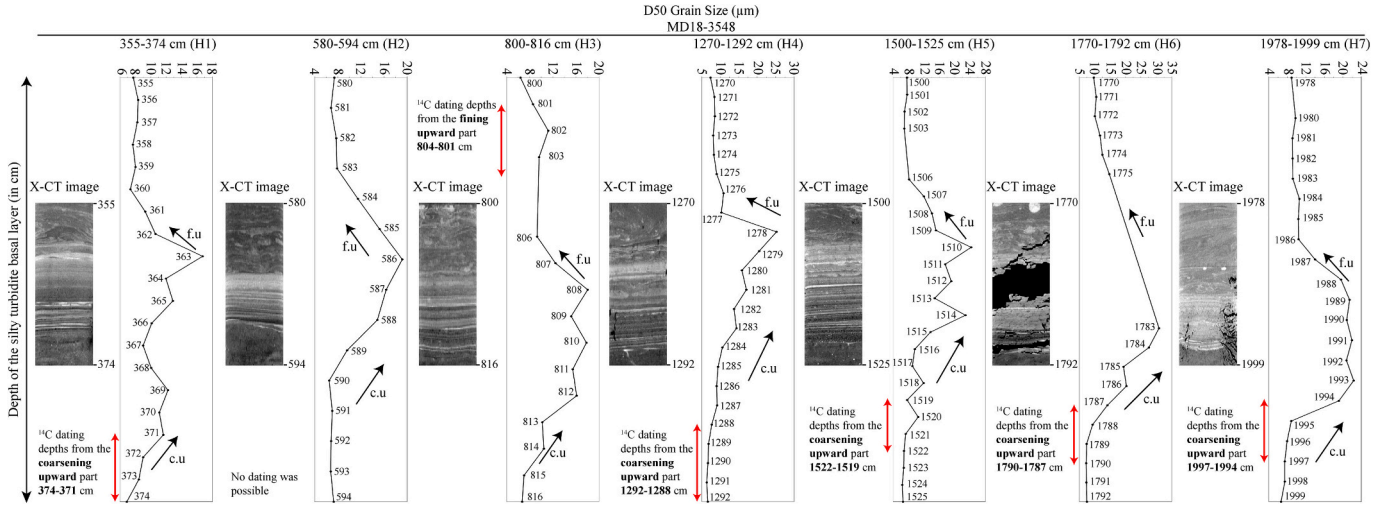

Fig. 6. D50 grain size of homogenite basal units (H1 to H7) from MD18–3548. All the basal units show a typical coarsening upward (c.u) and then fining upward (f.u) trend. The ^{14}C sampling depths for each homogenite basal unit is marked with a red arrow.

definitive trend (as exemplified in supplementary fig. 4).

Interpretation: The basal layer of homogenite shows parallel lamination, indicating tractional processes for deposition. The coarsening upward and then fining upward trend implies the waxing and waning condition of the flow. A gradational and non-erosive basal contact indicates a gradual change in flow and does not represent a surge flow, thereby differing significantly from a typical turbidity current. Basal layers are particularly enriched in foraminifers (up to 15–20 %), indicating that the sediments are most likely derived from marine realms rather than continental sources.

The thick upper layer is fine-grained silt without tractional features, indicating deposition from suspension. The homogeneous nature with

little vertical grain size variation as well as absence of bioturbation indicate rapid sedimentation from suspension. The slight yet noticeable fining upward trend may suggest the deposition of finer particles towards the end of the deposition. Moreover, all homogenite units are distinctly identified in CHIRP profiles as thick, transparent horizons (Fig. 3A, B, C). These layers typically resemble a blanket type of deposition, which are thicker in the basin centers and thin out towards the basin edges (Fig. 3B, C), indicating flow ponding.

3.1.3. Turbidites

Description: A total of four turbidite units (Fig. 4) are identified from the core (T1 to T4). These individual turbidite layers vary in thickness, ranging from 1 cm to ~14 cm. The turbidite beds typically exhibit a light greyish colour and are characterized by sharp bases that overlie the hemipelagic sediments. All the silty turbidite layers are normal graded and are enriched in foraminifera. The foraminifers within the turbidite were a mixture of both broken and well-preserved ones. The D50 grain size for MD18–3548, ranges from 7.29 μm (very fine silt) to 55.85 μm (coarse silt). They exhibit unimodal, bimodal and polymodal grain-size distributions (Fig. 5e). Sorting within these layers varies, spanning from poorly sorted to very poorly sorted. X-CT images reveal parallel lamination, and some traces of bioturbation (Fig. 5c). The density and magnetic susceptibility plots do not assist in differentiating the turbidites from the basal layer of the homogenites (e.g., supplementary fig. 4). Foraminifers in all four turbidite layers are randomly dispersed within the unit, and do not show the grading as seen in the basal layer of homogenites.

Interpretation: Identification of parallel laminae through X-CT images, indicate a tractional deposition process. Absence of bioturbation indicates rapid sedimentation of these event beds. Unlike the silty turbidite layers at the base of the homogenite, these turbidite layers do not exhibit the characteristic coarsening upward and fining upward trend and neither do the grading in foraminifera, attesting to a change in depositional processes between the two. Additionally, the layers above the turbidite exhibit low to moderate levels of bioturbation in hemipelagic sediments, contrasting sharply with the basal layer of the homogenite, which is overlain by very thick, non-bioturbated mud. All the turbidites belonging MD18–3548 correspond to the T3-T4 division of the Stow facies model, characterized by thin regular laminae or indistinct laminae (Stow and Smillie, 2020) and to the Tb division of the Bouma facies (Shanmugam, 1997).

3.1.4. Thin silty layers

Description: A total of six thin silty layers are identified throughout the core (Fig. 4). All the layers are 1–10 cm thick, and they appear as a contrast change in the X-CT images, compared to the overlying and underlying hemipelagites (Fig. 5d). The D50 grain size range from 6.9 μm (very fine silt) to 9.55 μm (fine silt). Sorting is not consistent for all the 6 layers, with some of them showing an abrupt difference (S2, S3, S5, and S6) and some not (S1 and S4). Similar to the turbidites, the density and magnetic susceptibility plots, and grain size distribution do not aid in delineating the thin silty layers from the turbidites or the basal layer of the homogenites (e.g., supplementary fig. 4). They also exhibit bimodal grain-size distribution (Fig. 5e). Without the aid of high-resolution grain size and X-CT images, it would be difficult to identify these event beds. Foraminifers (low concentration of broken and well-preserved) are present in three of the silt layers (S4, S5, and S6) and absent in the other three. Thin parallel laminae, devoid of bioturbation can be observed from the X-CT images of all the layers except the S1. Furthermore, a careful evaluation of certain silty layers was undertaken to verify the absence of volcanic glass shards (e.g., Supplementary fig. 5A, 5B).

Interpretation: The presence of thin, parallel silty laminae and an absence of bioturbation indicate a rapid sedimentation process facilitated by a weak tractional flow. We interpret that the weak tractional flow is the most likely mechanism and the lithofacies is similar to silty turbidite (T4 division) as reported by (Stow and Smillie, 2020) and also correspond to the Td division of Bouma facies (Shanmugam, 1997). Additionally, no volcanic glass shards were found (e.g., Supplementary fig. 5A, 5B).

3.2. AMS ^{14}C dating

The primary objectives of AMS ^{14}C dating is to establish a detailed age model of the core, calculate the rate of sedimentation (total rate and hemipelagic rate), and provide age intervals for event beds (silty turbidite-homogenites, turbidites, and thin silty layers). Dating from hemipelagic sediments was not feasible for the top 6 m due to the scarcity of foraminifera. Out of 'fourteen' samples, 'seven' of them were obtained from the basal layer of the homogenite (filled red circles in Fig. 7a) and are not used in the chronology reconstruction curve.

The coarsening-upward part of the basal layer of the homogenite shows a high concentration of foraminifera, typically within 2–3 cm thickness (except for H2 and H3). These depths were chosen for ^{14}C dating (Fig. 6). None of the samples from the hemipelagic section showed evidence of reworking (e.g., no broken foraminifers). All the samples were calibrated using the Calib 8.2 program (Stuiver and Reimer, 1993). The calibration was based on the MARINE20 curve (as outlined by Heaton et al., 2020). It is crucial to properly evaluate the radiocarbon marine reservoir effect when determining the absolute age of any material, such as planktonic foraminifera. Given the scarcity of data in offshore SW Taiwan (Yang et al., 2019; Yu et al., 2010), we applied the global average of the radiocarbon marine reservoir age, with the local reservoir age being, $\Delta r = 0$, to all the samples. The nominal background sedimentation rate was calculated exclusively from the hemipelagic layers, not considering the thickness of event beds.

The rate of hemipelagic sedimentation for MD18–3548 varies from 38 cm/kyr to 106 cm/kyr, averaging 74 cm/kyr. The youngest ^{14}C age for MD18–3548 from hemipelagic intervals is 3225 (3025–3398) cal yr BP at the depth of 6.55 m, the oldest obtained age is 11,593 (11,307–11,865) cal BP yr at a depth of 18.34 m (Table. 1).

4. Discussion

4.1. ^{14}C dating and rate of sedimentation

The rate of sedimentation is calculated for the entire core, and as well as the hemipelagic layers (Fig. 7a, b, and Table. 2). Sedimentation rates in the deep-water offshore SW Taiwan are generally <500 cm/kyr (Su et al., 2018). Cores from enclosed/semi-enclosed basins are expected to have low to moderate sedimentation rates, compared to those from canyons, which have high rates due to terrestrial sediment input. Of the 20.07 m length of MD18–3548, only 8.95 m belongs to hemipelagites, while the remaining 11.12 m belongs to sediments from event beds. Determining the exact boundary between hemipelagites and silty turbidite-homogenites, as well as the boundary between hemipelagites and turbidites (with the turbidite tail often being classified as hemipelagite), may not be possible. This uncertainty also extends to the distinction between hemipelagites and thin silty layers, leading to uncertainties in the thickness of each facies. Erosion is considered minimal, as all the turbidites vary from fine silt to coarse silt. Additionally, only two out of the seven homogenites with a silty basal layer (H2 and H7) units display a sharp base. The lowest hemipelagic sedimentation rate is recorded between 4095 and 3225 cal BP years (corresponding to depths of 8.46 m and 6.52 m), measuring 38.78 cm/kyr. Conversely, the highest sedimentation rate is observed between 10,650 and 9658 cal BP years (corresponding to depths of 16.28 m and 13.10 m), measuring 106.89 cm/kyr (Table 2). The nominal hemipelagic sedimentation rate for MD18–3548 is 74.52 cm/kyr, whereas the average rate of sedimentation for the entire core including event beds is 158.20 cm/kyr. Lin et al. (2014) have reported sedimentation rates from a semi-enclosed basin located northwest of our study area. The documented sedimentation rate

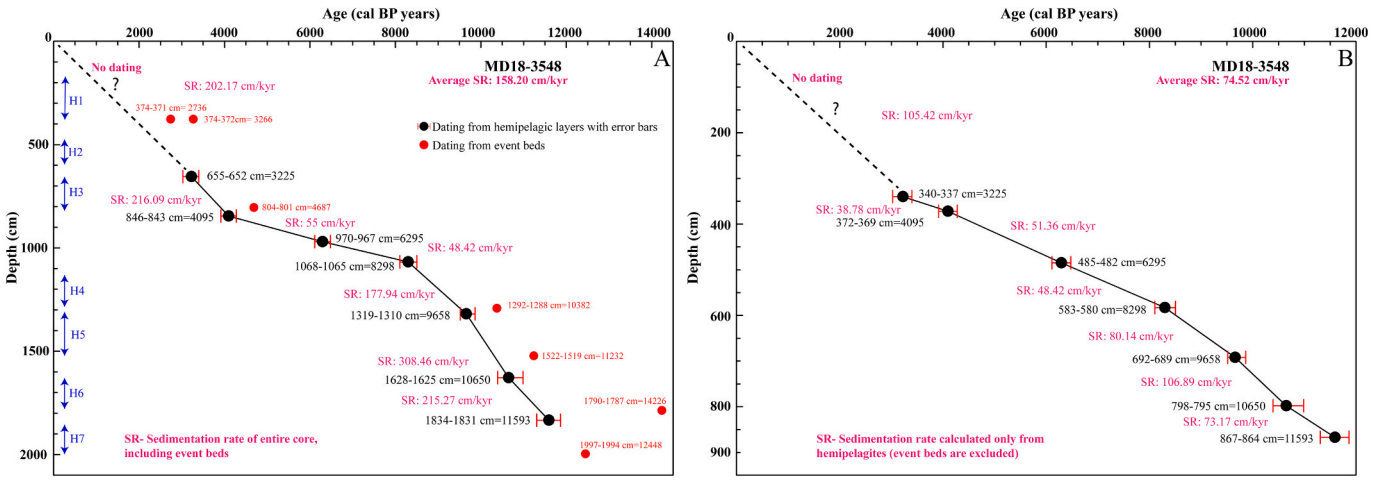

Fig. 7. (A) Chronological reconstruction of MD18–3548 based on ^{14}C AMS dating. Sedimentation rate (SR) is calculated for the entire core, including the event beds. (B) Chronological reconstruction of MD18–3548 removing all the event layers (depth recalculated only to hemipelagic intervals), and the Sedimentation rate (SR) is calculated only from hemipelagic sediments. Legend: Black filled circle and text: ^{14}C dating from hemipelagic layers; red filled circle and text: ^{14}C dating from basal layer of homogenite. All reported ages are in cal BP years. The extent of each silty turbidite-homogenite unit (H1 to H7) is shown on the depth axis.

Table 2
^{14}C AMS dating along with the rate of total sedimentation (including event beds) and hemipelagic sedimentation between those depths.

Depth in cm	2 σ cal BP median probability age	Total Sed. Rate, including event beds (cm/kyr)	Hemipelagic Sed. rate (cm/kyr)
652–655	3225	202.17	105.42
843–846	4095	216.09	38.78
967–970	6295	55	51.36
1065–1068	8298	48.42	48.42
1310–1319	9658	177.94	80.14
1625–1628	10,650	308.46	106.89
1831–1834	11,593	215.27	73.17
Average rate of sedimentation for entire core		158.20	74.52

for the past 12 ka ranges from 90 cm/kyr to 150 cm/kyr, with the top 2 ka showing a high sedimentation rate of 300 cm/kyr. These findings are consistent with the results of this study, suggesting that the giant piston core is likely intact, and any sediment loss in the top part of the core is minimal. Moreover, data obtained from piston and box cores from the southern Ryukyu forearc, collected during the same cruise leg, reveal a sediment loss of approximately 40 cm in piston cores (Babonneau et al., 2025). Assuming a similar loss of top sediments for our giant piston core, 40 cm thick would correspond to a loss of ~250 years.

4.2. *Dating of the silty turbidite-homogenite unit from reworked material*

In order to understand the maximum depths for the remobilized sediment source for the basal layers, radiocarbon dating was carried out at those reworked sediments. Given that our study area is a semi-enclosed basin devoid of terrestrial sediment input, we infer that the reworked sediments originate from the nearby seafloor. Hence the age difference between the emplacement ages of the event bed and the basal layer indicates the depth of sediments beneath the seafloor being remobilized. A total of seven samples corresponding to the basal layer were analyzed (Fig. 7a, Table 3). All the basal layers are enriched in foraminifers, with the exception of the H2 layer. Additionally, two dates were made possible for the H1 layer, one from foraminifera and the other from the tusk shell. It is not entirely unexpected for the tusk shell dating to be older (~ 500 yrs) than the age obtained from the foraminifers, as scaphopoda lives on the seafloor and feeds on foraminifera (Reynolds, 2002). However, it should be noted that some degree of

Table 3
Calculation of the assumed maximum remobilized depth of sediments (from both seafloor and slope sediments) is based on ^{14}C AMS dating results of basal layer of homogenite, actual age of the event beds based on rate of hemipelagic sedimentation, and the age differences calculated from the rate of hemipelagic sedimentation. Abbreviations: BFS-Basin Floor Sediments.

Depth in cm, corresponding basal layer	^{14}C 2 σ cal BP median probability age	Emplacement age based on rate of hemipelagic sedimentation	Age difference	Assumed maximum remobilized depth of sediments, in cm
371–374, H1	2736	1698	1038	~79 (BFS) ~40 (Slope + BFS)
372–376, H1 (tusk shell)	3266	1698	1568	~120 (BFS) ~60 (Slope + BFS)
802–804, H3	4687	3361	1326	~102 (BFS) ~51 (Slope + BFS)
1288–1292, H4	10,382	9322	1060	~81 (BFS) ~40 (Slope + BFS)
1519–1522, H5	11,232	9743	1489	~114 (BFS) ~57 (Slope + BFS)
1787–1790, H6	14,226	11,019	3207	~246 (BFS) ~123 (Slope + BFS)
1994–1997, H7	12,448	12,085	363	~27 (BFS) ~13 (Slope + BFS)

uncertainty may exist regarding the depositional ages of H1 and H2, as no hemipelagic AMS ^{14}C dating was possible for the top 6 m of the core. The age differences between the ^{14}C age from reworked material and the estimated emplacement age of the event bed as calculated from the rate of hemipelagic sedimentation, is outlined in Table 3. This age difference gives a rough estimate for maximum depths of sediment remobilization beneath the seafloor. The maximum depths of assumed basinal sediment remobilization, excluding the H6 layer, range from 27 cm to 114 cm. The corresponding age differences ranges from ~1000 years to ~1500 years, with two outliers falling at 363 years (H7) and 3207 years (H6). The thinning of the basin sediments onto the basin margin and slope suggests that the sedimentation rate on the slope is much lower than that

on the basin floor (Fig. 3B, C), possibly being one-half or one-third on the slope. Assuming one-half, the depth of sediments being remobilized for the entire basin is calculated (Table 3). The recalculated depths for all the layers are probably within a reasonable estimate, ranging from 13 cm to 57 cm, with H6 layer being the sole outlier at 123 cm. This suggests that the source sediments for the homogenite unit are derived from both the resuspension of basin floor sediments and the remobilization of slope sediments.

4.3. Depositional model for silty turbidite-homogenite units

The crucial criteria for the deposition of homogenites are the presence of enclosed or semi-enclosed basins (Stanley, 1981), which facilitate trapping of the sediment clouds. The SW offshore region of Taiwan has many such localized basins, making them ideal sites for homogenite deposition. We propose a new three-stage model for the deposition of silty turbidite-homogenites (Fig. 8). This model, which is based on high-resolution grain size data and X-CT images, facilitates a better explanation for the massive event beds in the core MD18–3548.

Table 4
Determining criteria for the event beds and defining the upper and lower limits for event beds in MD18–3548.

Event bed	Upper-lower range (in cm), total thickness of the event bed	Identifying criteria for the event bed
S1	6–7, 2 cm	Grain size, sorting, and X-CT image
S2	25, 1 cm	Grain size, sorting, and X-CT image
S3	172, 1 cm	Grain size, sorting, and X-CT image
H1	173–374, 201 cm Homogenite layer: 182 cm; Silty basal layer: 19 cm (12 cm coarsening upward, 8 cm fining upward)	X-CT image, grain size and sudden change in sorting
H2	490–594, 104 cm Homogenite layer: 89 cm; Silty basal layer: 15 cm (9 cm coarsening upward, 6 cm fining upward)	X-CT image, and grain size
H3	660–816, 156 cm Homogenite layer: 139 cm; Silty basal layer: 17 cm (9 cm coarsening upward, 8 cm fining upward)	X-CT image, grain size and sudden change in sorting
S4	855–865, 10 cm	Grain size, sorting, and X-CT image
T1	883–886, 4 cm	Grain size, sorting, and X-CT image
T2	995, 1 cm	Grain size, sorting, and X-CT image
T3	1075–1083, 8 cm	Grain size, sorting, and X-CT image
H4	1150–1292, 142 cm Homogenite layer: 119 cm; Silty basal layer: 23 cm (15 cm coarsening upward, 8 cm fining upward)	X-CT image, grain size and sudden change in sorting
H5	1325–1525, 200 cm Homogenite layer: 174 cm; Silty basal layer: 26 cm (16 cm coarsening upward, 10 cm fining upward)	X-CT image, grain size and sudden change in sorting
S5	1546–1547, 2 cm	Grain size, sorting, and X-CT image
T4	1575–1589, 14 cm	Grain size, sorting, and X-CT image
S6	1610, 1 cm	Grain size, sorting, and X-CT image
H6	1655–1792, 137 cm Homogenite layer: 114 cm; Silty basal layer: 23 cm (10 cm coarsening upward, 13 cm fining upward)	X-CT image, grain size and sudden change in sorting
H7	1870–1999, 129 cm Homogenite layer: 107 cm; Silty basal layer: 22 cm (9 cm coarsening upward, 13 cm fining upward)	X-CT image, grain size and sudden change in sorting

1) A silty turbidite layer (basal layer) that is coarsening-upward to fining-upward. This stage involves initiation and trigger of the flow, transportation of sediments and deposition (traction) of the silty basal layer.
2) A uniform and thick structureless layer, called the homogenite (upper layer). This stage involves deposition of the homogenite through suspension fall-out.
3) The deposition of hemipelagic sediments on top of the homogenite layer.

4.3.1. Stage 1 A and 1B- Remobilization and silty turbidite layer deposition stage

The slope remobilization concept is documented by Ashi et al. (2014), Moernaut et al. (2017), McHugh et al. (2016; 2020), Molenaar et al. (2019). Ashi et al. (2014) speculated that the 2-m thick turbid layer recognized in a terminal and enclosed basin floor of Nankai accretionary prism is a result of surficial slope sediment remobilization. Earthquake ground motion remobilized the source sediments and homogenized into synchronous muddy mass flows that were transported over wide areas of the seafloor (ponding on mid-slope terraces and numerous small basins), resulting in deposits as much as 200 cm thick (McHugh et al., 2016). Ashi et al. (2012) reported the occurrence of a dilute suspension layer (DSL) and a bottom turbid layer (BTL) following the 2004 Kii Peninsula earthquakes. The authors further noted that turbidity measurements of seafloor taken six years later indicated that the BTL was 2.4 m thick, suggesting extensive sediment redistribution and remobilization as a result of seismic activity shortly after the earthquake. ROV (remotely operated underwater vehicle) observations made soon after the 2004 Kii peninsular earthquake (Ashi et al., 2014), and 2011 Tohoku-Oki earthquake (Oguri et al., 2013), observed high turbidity in the bottom waters of the Japan Trench. A 600 m thick suspension cloud was found in the Puerto Rican Trench, several months after the 2010 Haiti earthquake (McHugh et al., 2011, 2016) indicating that suspension cloud deposits are responsible for the deposition of the massive upper layer of homogenite beds.

We propose that the seafloor experiences severe shaking, most likely due to great earthquakes. The shaking of the seafloor leads to remobilizing the top layer of slope sediments and simultaneously resuspending the basin-floor sediments (Schwestermann et al., 2020). The remobilized slope sediments cascade down towards the basin floor and result in the formation of a benthic nepheloid layer. Part of this layer may further develop into intermediate nepheloid layers, possibly extending to the entire width of the basin. Similar concept of sediment remobilization due to earthquakes was previously reported by Ikehara et al. (2020), with focus on Japan trench earthquakes, Okutsu et al. (2019) in the Nanakai forearc region, as well as by Noguchi et al. (2012) and Oguri et al. (2013) in relation to the 2011 Tohoku-oki earthquake.

These benthic nepheloid layers, which contain coarser fraction sediments due to density differences, travel downwards and accelerate in velocity due to flow turbulence. This process also entrains seafloor sediments into the layer, leading the benthic layers to become an initially slow-moving gravity flow. The gain in acceleration of velocity of flow is the ‘waxing stage’ (Fig. 8, Stage 1 A). This stage results in an increase in grain size from finer to coarser, and the acceleration reaches its peak, facilitating the deposition of a coarsening-upward layer enriched in foraminifers. As the flow velocity decreases, the ‘waning stage’, a fining-upward layer with relatively less foraminifers, is deposited. This sequence of a coarsening-upward layer, followed by the fining-upward layer is referred to as the basal layer (Fig. 8, Stage 1B), reflecting the development of a waxing to waning gravity-driven tractional flows. Our model also explains the vertical variation in the concentration of foraminifera at the basal layer. The foraminifera in the basal layer originates from the remobilization and resuspension of slope sediments and basin floor sediments. The foraminifera exhibits a higher concentration at the base of the basal layer and gradually decreases

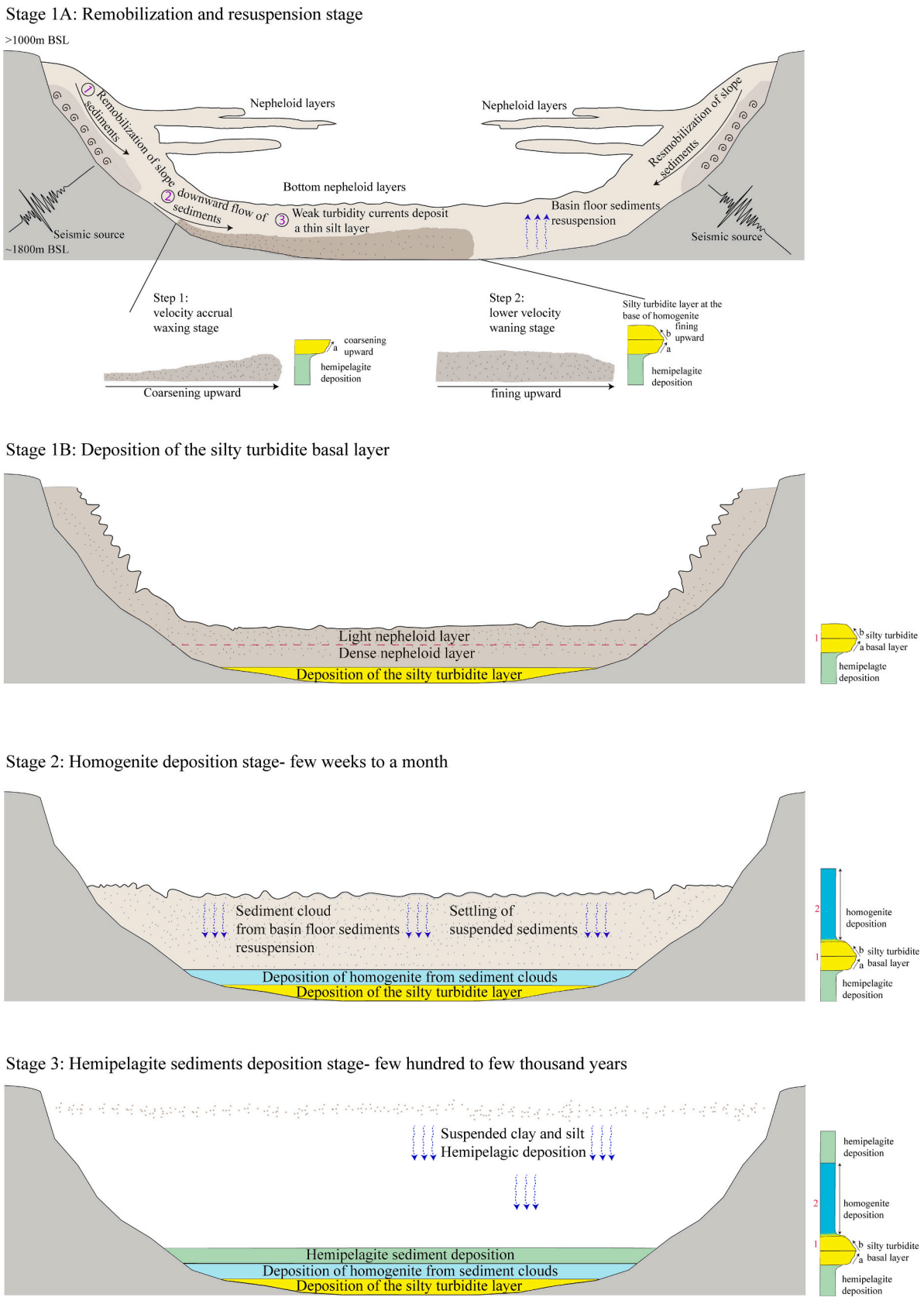

Fig. 8. A three-stage model for deposition of silty turbidite-homogenites in a perched basin setting. The model is not to scale.

upward as the flow energy diminishes.

4.3.2. Stage 2-Homogenite deposition stage: a few weeks to a few months

The ponded basin water is now clouded with very fine-grained sediments sourced from nepheloid layers. These sediments, through suspension fall-out, are responsible for the continuous and rapid deposition of very fine-grained sediments (ranging from very fine silt to fine silt). The timeframe required for the deposition of fine silts from suspension sediment clouds is estimated from Stokes' Law (e.g., Eq. 1, supplementary data; Moran, 2018).

The resultant deposit is a 1–2 m thick, nearly uniform, structureless unit, devoid of foraminifers, and without bioturbation, called the upper layer (Fig. 8, Stage 2). Both the basal layer (Stage 1) and the upper layer (Stage 2) together comprise a single 'silty turbidite-homogenite' unit.

4.3.3. Stage 3-Hemipelagite sediments deposition stage: a few hundred to a few thousand years

After the entire unit of homogenite has been deposited through suspension fall-out, particles of clay-silt size are deposited. These are called hemipelagites and they overlie homogenites. The rate of deposition of hemipelagites is much slower than that of the upper layer, resulting in moderate to intense bioturbation and presence of foraminifera. The nominal rate of hemipelagic sedimentation for our core is 74.52 cm/kyr (Fig. 7B), with the interval between each homogenite with a silty basal layer ranging from ~400 to 6000 years.

4.4. Comparison with other potential flows

Mulder et al. (2001) reports flood triggered hyperpycnal turbidity currents from the Var turbidite system, located in the Ligurian Sea, NW Mediterranean. The study describes a coarsening-upward basal unit, followed by a fining-upward unit, separated by a contact, either gradational or erosional. No such sharp contact exists in our homogenite basal layer. Hyperpycnal turbidity currents are capable of traveling long distances, particularly with particles finer than sand (Mulder and Syvitski, 1995). There are reports of hyperpycnal turbidity currents occurring in offshore SW Taiwan (Sparkes et al., 2015), where the currents are confined within the drainage of the Gaoping Cayon. Our studied perched basin is around 30 km away from the Gaoping Canyon and is separated from the canyon with an array of significant bathymetric highs (Fig. 1). It is therefore highly unlikely that hyperpyncal turbidity currents would reach the studied perched basin and lead to homogenite deposition in the study area.

Contourites and sediment waves have been documented in offshore southwestern Taiwan (Gong et al., 2012; Chen et al., 2024). Contourites may also demonstrate both coarsening upward and fining upward sequences as a result of changing velocity of the bottom currents (Stow et al., 2002). Unlike the homogenites from our study, contourites are typically extensively bioturbated and may exhibit distinct burrows, characteristics of deep water ichnofacies (Wetzel et al., 2008). They also form over a longer time scales, usually more than a few thousand years (Smillie et al., 2019), unlike our homogenites, which are deposited instantaneously.

4.5. Homogenites from offshore SW Taiwan

Deepwater homogenites or turbidite-homogenite sequences, with various triggering and depositional mechanisms, are well-documented in other regions of the world (Hieke, 1984; Hieke and Werner, 2000; Kastens and Cita, 1981; Kastens, 1984; Cita et al., 1984; Cita, 2008; Shiki and Cita, 2008; Beck et al. (2007, 2012); Beck, 2009; Tripsanas et al., 2004; Campos et al., 2013; Yakupoğlu et al., 2022; Jones et al., 1992; McHugh et al. (2006, 2020); San Pedro et al., 2017; Chapron et al., 1999; Guyard et al., 2007; Polonia et al. (2013, 2016, 2017, 2022); St-Onge et al., 2012; Kong et al., 2019). A summary of facies comparison with our study area is provided in Fig. 9.

Such stark similarities from various geological settings around the world advocate that homogenites are event deposits of seismic origin and are deposited from the surficial remobilization and resuspension of both basin floor sediments and slope sediments. In our study area, offshore SW Taiwan, we have a similar observation. The homogenite layers are clearly identified from high-resolution sub-bottom profiles. Basin-scale CHIRP profiles (NW-SE and SW-NE) crossing the MD18–3548 site reveal an extraordinary continuity of reflection-free, thick transparent layers across flat basin plains, while the reflectors thin out or wedge out at the basin margins (Fig. 3B, C).

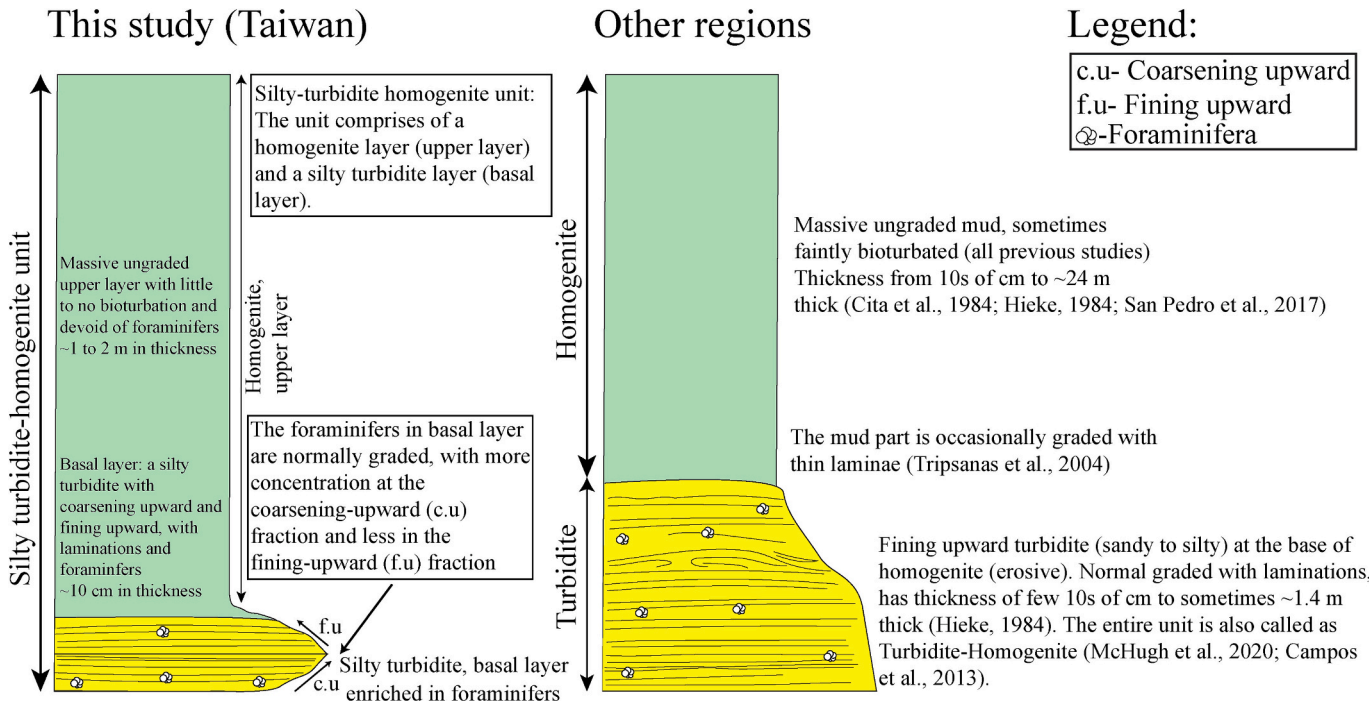

Fig. 9. Comparison of lithofacies of 'silty turbidite-homogenite units' found in offshore SW Taiwan with those in other regions.

In our perched basin setting (Fig. 2), sediment sources are not confined to this basin margin alone; additional probable sediment sources may originate from the elongated slope basins, given their interconnected depressions. Cascading nepheloid layers might overspill the topographic highs, and some of the bottom nepheloid layers may escape through the two small outlets, resulting in a reduced thickness of the muddy event bed.

All the above-mentioned studies from various geological settings are partially in coherence with our observation in offshore southwestern Taiwan. However, the major differences we observe are in regard to the sedimentary characteristics of the homogenites, and the depositional models. For lithofacies, most agree with the existence of two distinct process of deposition for homogenite, i.e. presence of a basal turbidite layer and an upper homogenous layer, differing in lithology and deposition process. However, the major difference we observe in sedimentary characteristics is the clear identification of a gradual coarsening upward trend, followed by a fining upward trend, that further gradually merges with the upper layer of the homogenite. In contrast, in turbidites associated with homogenites, only the fining-upward layer is being reported in other studies. The erosive and fining-upward basal layer from previous studies are interpreted to be as a result from surge-type turbidity currents, triggered by slope failures. In contrast, our silty turbidite basal layer, show a non-erosive, gradual coarsening-upward trend, indicative of a non-surge type and a waxing tractional flow.

5. Conclusions

Silty turbidite-homogenite units are reported for the first time from a perched basin, offshore SW Taiwan. A total of fourteen samples were chosen for ^{14}C AMS dating, seven of which were from event beds and seven from the hemipelagic layers. The average rate of sedimentation for MD18–3548 is ~75 cm/kyr.

Detailed sedimentological investigations based on high-resolution grain size and X-CT images, coupled with CHIRP data, reveal four major facies in MD18–3548. They are: hemipelagic sediments, silty turbidite-homogenite units, turbidites, and thin silty layers. In total, 17 event beds have been identified, 7 belonging to silty turbidite-homogenite units, 4 to turbidites, and 6 to thin silty layers. Silty turbidite-homogenite units account for ~54 % of the entire core length. In CHIRP data, these units appear as thick, transparent layers that concentrate in flat basin plains and pinch out towards the basin edge. The X-CT images reveal that the upper homogenous units are thick (1–2 m), mostly unbioturbated, and devoid of forams. In contrast, the basal layer are 10–20 cm in thickness, show parallel lamination, and contain abundant foraminfera. This basal layer typically exhibits a coarsening upward and fining upward trend. Although our results are consistent with previous studies suggesting that homogenite units are deposited from the remobilization of slope sediments and resuspension of basin floor sediments (seismogenic triggered), none of these studies emphasize the presence of this coarsening-upward and fining-upward trend in the silty turbidite layer at the base of the homogenite. Previous studies have identified that the majority of turbidite units located at the base of homogenites consist of sandy sediments. In contrast, our study reveals that all turbidites at the base of homogenites are silty. Consequently, we designate these as silty turbidite-homogenite units. Accurate facies classification is essential, as the observed coarsening-upward sequence followed by the fining-upward sequence is likely attributable to the predominantly silty nature of the sediments, indicating deposition in a lower energy regime. Thereby, we propose a new depositional model for the newly identified silty turbidite-homogenite units in enclosed/semi-enclosed basins. Offshore SW Taiwan acts as a natural laboratory with its numerous localized perched basins. This setting enables further studies, which are essential to address various questions, including the recurrence intervals of homogenite beds, the faults responsible for their formation, and comparisons of such seismic events with historical records.

Supplementary data to this article can be found online at https://doi.org/10.1016/j.sedgeo.2025.106854.

CRediT authorship contribution statement

Radha Krishna Pillutla: Writing – original draft, Visualization, Methodology, Investigation, Formal analysis, Data curation. **Andrew Tien-Shun Lin:** Writing – review & editing, Supervision, Software, Resources, Project administration, Funding acquisition, Conceptualization. **Jen-Chu Yeh:** Investigation, Formal analysis, Data curation. **Gueorgui Ratzov:** Writing – review & editing, Validation, Methodology, Funding acquisition. **Nathalie Babonneau:** Writing – review & editing, Validation, Methodology, Funding acquisition. **Shu-Kun Hsu:** Resources, Funding acquisition. **Chih-Chieh Su:** Resources, Funding acquisition. **Serge Lallemand:** Resources, Funding acquisition, Data curation. **Ludvig Löwemark:** Writing – review & editing.

Declaration of competing interest

The authors declare that there is no finacial/personal interest or belief that could affect the objectivity of this manuscript.

Acknowledgements

We would like to thank the crew, shipboard scientists, and the technical team of R/V *Marion* Dufresne, during MD214/EAGER cruise, partially funded by the National Energy Program-Phase II (NEPII) project of National Science and Technology Council (NSTC) of Taiwan and supported by the International Research Project (IRP): From Deep Earth to Extreme Events (D3E) between Centre National de la Recherche Scientifique (CNRS) of France and NSTC of Taiwan. We also thank the French Research Institution, such as the French Oceanographic Fleet (FOF), IFREMER, GENAVIR, CNRS, and the French universities associated with the EAGER project. This study was funded by NSTC under the grant MOST 110-2611-M-008-004 and NSTC 111-2611-M-008-009. This work was also financially supported by the "The Featured Areas Research Center Program" within the framework of the Higher Education Sprout Project by the Ministry of Education in Taiwan. We also thank the AMS lab at National Taiwan University (NTUAMS) for facilitating the carbon dating and the Taiwan Instrument Research Institute (TIRI), located in Hsinchu Science and Industrial Park, Taiwan, for the CT scanning of all the cores. We also acknowledge the financial support received from TIGP (Taiwan International Graduate Program). We also extend our gratitude to the reviewers and the editor for their invaluable time and insightful comments.

Data availability

Grain size analysis (Original data) (Mendeley Data)

References

Ashi, J., Ikehara, K., Kinoshita, M., 2012. Settling of earthquake-induced turbidity on the accretionary prism slope of the central Nankai subduction zone. In: Submarine Mass Movements and their Consequences. Springer, Netherlands, pp. 561–571. https://doi.org/10.1007/978-94-007-2162-3_50.

Ashi, J., Sawada, R., Omura, A., Ikehara, K., 2014. Accumulation of an earthquake-induced extremely turbid layer in a terminal basin of the Nankai accretionary prism. Earth, Planets and Space 66 (1), 51. https://doi.org/10.1186/1880-5981-66-51.

Babonneau, N., Ratzov, G., Guerin, C., Richa, M., Lallemand, S., Condomines, M., Bachelery, P., Bosch, D., Hsu, S.-K., Su, C.-C., Shinjo, R., Lin, A. T.-S., Bassetti, M.-A., Revel, M., Cattaneo, A., and the EAGER scientific team. (2025). Sedimentary record of deep submarine gravity-flow events in the southern Ryukyu forearc during the last 200,000 years: archive of mega-earthquakes and tsunamis. Submitted to Sedimentology (under revision).

Beck, C., 2009. Late Quaternary lacustrine paleo-seismic archives in North-Western Alps: examples of earthquake-origin assessment of sedimentary disturbances. Earth-Science Reviews 96, 327–344. https://doi.org/10.1016/j.earscirev.2009.07.005.

Beck, C., Mercier de Lépinay, B., Schneider, J.-L., Cremer, M., Çağatay, N., Wendenbaum, E., Boutareaud, S., Ménot, G., Schmidt, S., Weber, O., Eris, K.,

Armijo, R., Meyer, B., Pondard, N., Gutscher, M.-A., Turon, J.-L., Labeyrie, L., Cortijo, E., Gallet, Y., Jaouen, A., 2007. Late Quaternary co-seismic sedimentation in the Sea of Marmara's deep basins. Sedimentary Geology 199 (1–2), 65–89. https://doi.org/10.1016/j.sedgeo.2005.12.031.

Beck, C., Reyss, J.-L., Leclerc, F., Moreno, E., Feuillet, N., Barrier, L., Beauducel, F., Boudon, G., Clément, V., Deplus, C., Gallou, N., Lebrun, J.-F., Le Friant, A., Nercessian, A., Paterne, M., Pichot, T., Vidal, C., 2012. Identification of deep subaqueous co-seismic scarps through specific coeval sedimentation in Lesser Antilles: implication for seismic hazard. Natural Hazards and Earth System Sciences 12 (5), 1755–1767. https://doi.org/10.5194/nhess-12-1755-2012.

Bellon, H., Yumul, G., 2000. Mio-Pliocene magmatism in the Baguio mining district (Luzon, Philippines): age clues to its geodynamic setting. Comptes Rendus de l'Académie des Sciences - Series IIA - Earth and Planetary Science 331 (4), 295–302. https://doi.org/10.1016/S1251-8050(00)01415-4.

Bertrand, S., Charlet, F., Chapron, E., Fagel, N., de Batist, M., 2008. Reconstruction of the Holocene seismotectonic activity of the Southern Andes from seismites recorded in Lago Icalma, Chile, 39°S. Palaeogeography, Palaeoclimatology, Palaeoecology 259 (2–3), 301–322. https://doi.org/10.1016/j.palaeo.2007.10.013.

Blott, S.J., Pye, K., 2001. GRADISTAT: a grain size distribution and statistics package for the analysis of unconsolidated sediments. Earth Surface Processes and Landforms 26 (11), 1237–1248. https://doi.org/10.1002/esp.261.

Çağatay, M.N., Erel, L., Bellucci, L.G., Polonia, A., Gasperini, L., Eriş, K.K., Sancar, Ü., Biltekin, D., Uçarkuş, G., Ülgen, U.B., Damcı, E., 2012. Sedimentary earthquake records in the İzmit Gulf, Sea of Marmara, Turkey. Sedimentary Geology 282, 347–359. https://doi.org/10.1016/j.sedgeo.2012.10.001.

Campos, C., Beck, C., Crouzet, C., Demory, F., van Welden, A., Eris, K., 2013. Deciphering hemipelagites from homogenites through anisotropy of magnetic susceptibility. Paleoseismic implications (Sea of Marmara and Gulf of Corinth). Sedimentary Geology 292, 1–14. https://doi.org/10.1016/j.sedgeo.2013.03.015.

Carrillo, E., Beck, C., Audemard, F.A., Moreno, E., Ollarves, R., 2008. Disentangling late Quaternary climatic and seismo-tectonic controls on Lake Mucubají sedimentation (Mérida Andes, Venezuela). Palaeogeography, Palaeoclimatology, Palaeoecology 259 (2–3), 284–300. https://doi.org/10.1016/j.palaeo.2007.10.012.

Cattaneo, A., Badhani, S., Caradonna, C., Bellucci, M., Leroux, E., Babonneau, N., Garziglia, S., Poort, J., Akhmanov, G.G., Bayon, G., Dennielou, B., Jouet, G., Migeon, S., Rabineau, M., Droz, L., Clare, M., 2020. The last Glacial Maximum Balearic Abyssal Plain megabed revisited. Geological Society, London, Special Publications 500 (1), 341–357. https://doi.org/10.1144/SP500-2019-188.

Chapron, E., Beck, C., Pourchet, M., Deconinck, J., 1999. 1822 earthquake-triggered homogenite in Lake Le Bourget (NW Alps). Terra Nova 11 (2–3), 86–92. https://doi.org/10.1046/j.1365-3121.1999.00230.x.

Chen, K.-T., Hsu, S.-K., Lin, A.T.-S., Su, C.-C., Babonneau, N., Ratzov, G., Lallemand, S., Huang, P.-C., Lin, L.-K., Lin, H.-S., Tsai, C.-H., Lin, J.-Y., Chen, S.-C., 2024. Changes in marine sedimentation patterns in the northeastern South China Sea in the past 35,000 years. Communications Earth & Environment 5 (1), 420. https://doi.org/10.1038/s43247-024-01593-3.

Chen, P.-F., Newman, A., v., Wu, T.-R., Lin, C.-C., 2008. Earthquake probabilities and energy characteristics of seismicity offshore Southwest Taiwan. Terrestrial, Atmospheric and Oceanic Sciences 19 (6), 697. https://doi.org/10.3319/TAO.2008.19.6.697(PT).

Chuang, P.-C., Dale, A.W., Wallmann, K., Haeckel, M., Yang, T.F., Chen, N.-C., Chen, H.-C., Chen, H.-W., Lin, S., Sun, C.-H., You, C.-F., Horng, C.-S., Wang, Y., Chung, S.-H., 2013. Relating sulfate and methane dynamics to geology: Accretionary prism offshore SW Taiwan. Geochemisty, Geophysics, Geosystems 14, 2523–2545. https://doi.org/10.1002/ggge.20168.

Cita, M.B., 2008. Deep- Sea Homogenites: Sedimentary expression of a prehistoric megatsunami in the eastern Mediterranean. In: Tsunamiites. Elsevier, pp. 185–202. https://doi.org/10.1016/B978-0-444-51552-0.00012-6.

Cita, M.B., Camerlenghi, A., Kastens, K.A., McCoy, F.W., 1984. New findings of Bronze Age homogenites in the Ionian Sea: Geodynamic implications for the Mediterranean. Marine Geology 55 (1–2), 47–62. https://doi.org/10.1016/0025-3227(84)90132-4.

Cita, M.B., Camerlenghi, A., Rimoldi, B., 1996. Deep-sea tsunami deposits in the eastern Mediterranean: New evidence and depositional models. Sedimentary Geology 104 (1–4), 155–173. https://doi.org/10.1016/0037-0738(95)00126-3.

Dadson, S.J., Hovius, N., Chen, H., Dade, W.B., Hsieh, M.L., Willett, S.D., Hu, J.C., Horng, M.J., Chen, M.C., Stark, C.P., Lague, D., Lin, J.C., 2003. Links between erosion, runoff variability and seismicity in the Taiwan orogen. Nature 426, 648–651. https://doi.org/10.1038/nature02150.

Folk, R.L., Ward, W.C., 1957. Brazos River bar [Texas]; a study in the significance of grain size parameters. Journal of Sedimentary Research 27 (1), 3–26. https://doi.org/10.1306/74D70646-2B21-11D7-8648000102C1865D.

Fuller, M., McCabe, R., Williams, I.S., Almasco, J., Encina, R.Y., Zanoria, A.S., Wolfe, J. A., 1983. Paleomagnetism of Luzon. American Geophysical Union Geophysical Monograph 27, 79–94. https://doi.org/10.1029/GM027p0079.

Gong, C., Wang, Y., Peng, X., Li, W., Qiu, Y., Xu, S., 2012. Sediment waves on the South China Sea Slope off southwestern Taiwan: Implications for the intrusion of the Northern Pacific Deep Water into the South China Sea. Marine and Petroleum Geology 32 (1), 95–109. https://doi.org/10.1016/j.marpetgeo.2011.12.005.

Guyard, H., St-Onge, G., Chapron, E., Anselmetti, F.S., Francus, P., 2007. The AD 1881 earthquake-triggered slump and late holocene flood-induced turbidites from proglacial lake Bramant, Western French alps. In: Submarine Mass Movements and their Consequences. Springer, Netherlands, pp. 279–286. https://doi.org/10.1007/978-1-4020-6512-5_29.

Heaton, T.J., Köhler, P., Butzin, M., Bard, E., Reimer, R.W., Austin, W.E.N., Bronk Ramsey, C., Grootes, P.M., Hughen, K.A., Kromer, B., Reimer, P.J., Adkins, J., Burke, A., Cook, M.S., Olsen, J., Skinner, L.C., 2020. Marine20—the marine radiocarbon age calibration curve (0–55,000 cal BP). Radiocarbon 62 (4), 779–820. https://doi.org/10.1017/RDC.2020.68.

Hieke, W., 1984. A thick Holocene homogenite from the Ionian Abyssal plain (eastern Mediterranean). Marine Geology 55 (1–2), 63–78. https://doi.org/10.1016/0025-3227(84)90133-6.

Hieke, W., Werner, F., 2000. The Augias megaturbidite in the central Ionian Sea (Central Mediterranean) and its relation to the Holocene Santorini event. Sedimentary Geology 135 (1–4), 205–218. https://doi.org/10.1016/S0037-0738(00)00072-5.

Huang, J., Wan, S., Xiong, Z., Zhao, D., Liu, X., Li, A., Li, T., 2016. Geochemical records of Taiwan-sourced sediments in the South China Sea linked to Holocene climate changes. Palaeogeography, Paleoclimatology, Paleoecology 441, 871–881. https://doi.org/10.1016/j.palaeo.2015.10.036.

Huang, Y.-S., Hsu, S.-K., Su, C.-C., Lin, A.T.-S., Yu, P.-S., Babonneau, N., Ratzov, G., Lallemand, S., Huang, P.-C., Lin, S.-S., Lin, J.-Y., Wei, K.-Y., Chang, Y.-P., Yu, N.-T., Tsai, C.-H., 2021. Shallow gas hydrates off Southwest Taiwan and their mechanisms. Marine Geophysical Research 42 (1), 7. https://doi.org/10.1007/s11001-021-09429-x.

Hutchings, S.J., Mooney, W.D., 2024. Seismotectonics of the Philippine and Taiwan subduction systems and implications for seismic hazards. Geochemistry, Geophysics, Geosystems 25 (6). https://doi.org/10.1029/2023GC010990.

Ikehara, K., Kanamatsu, T., Nagahashi, Y., Strasser, M., Fink, H., Usami, K., Irino, T., Wefer, G., 2016. Documenting large earthquakes similar to the 2011 Tohoku-oki earthquake from sediments deposited in the Japan Trench over the past 1500 years. Earth and Planetary Science Letters 445, 48–56. https://doi.org/10.1016/j.epsl.2016.04.009.

Ikehara, K., Usami, K., Kanamatsu, T., 2020. Repeated occurrence of surface-sediment remobilization along the landward slope of the Japan Trench by great earthquakes. Earth, Planets and Space 72 (1), 114. https://doi.org/10.1186/s40623-020-01241-y.

Ikehara, K., Usami, K., Irino, T., Omura, A., Jenkins, R.G., Ashi, J., 2021. Characteristics and distribution of the event deposits induced by the 2011 Tohoku-oki earthquake and tsunami offshore of Sanriku and Sendai. Japan. Sedimentary Geology 411, 105791. https://doi.org/10.1016/j.sedgeo.2020.105791.

Jones, K.P.N., McCave, I.N., Weaver, P.P.E., 1992. Textural and dispersal patterns of thick mud turbidites from the Madeira Abyssal plain. Marine Geology 107 (3), 149–173. https://doi.org/10.1016/0025-3227(92)90165-E.

Kanamatsu, T., Ikehara, K., Hsiung, K.-H., 2023. Submarine paleoseismology in the Japan Trench of northeastern Japan: turbidite stratigraphy and sedimentology using paleomagnetic and rock magnetic analyses. Progress in Earth and Planetary Science 10 (1), 16. https://doi.org/10.1186/s40645-023-00545-3.

Kastens, K.A., 1984. Earthquakes as a triggering mechanism for debris flows and turbidites on the Calabrian Ridge. Marine Geology 55 (1–2), 13–33. https://doi.org/10.1016/0025-3227(84)90130-0.

Kastens, K.A., Cita, M.B., 1981. Tsunami-induced sediment transport in the abyssal Mediterranean Sea. Geological Society of America Bulletin 92 (11), 845–857. https://doi.org/10.1130/0016-7606(1981)92<845:TSTITA>2.0.CO;2.

Kong, X., Jiang, Z., Han, C., Li, H., Li, Q., Zheng, L., Yang, Y., Zhang, J., Xiao, F., 2019. Sedimentary characteristics and depositional models of two types of homogenites in an Eocene continental lake basin, Shulu Sag, eastern China. Journal of Asian Earth Sciences 179, 165–188. https://doi.org/10.1016/j.jseaes.2019.04.023.

Krumbein, W.C., 1938. Size frequency distributions of sediments and the normal phi curve. SEPM Journal of Sedimentary Research 8 (3), 84–90. https://doi.org/10.1306/D4269008-2B26-11D7-8648000102C1865D.

Lacombe, O., Mouthereau, F., Angelier, J., Deffontaines, B., 2001. Structural, geodetic and seismological evidence for tectonic escape in SW Taiwan. Tectonophysics 333 (1–2), 323–345. https://doi.org/10.1016/S0040-1951(00)00281-X.

Li, C., Shi, X., Kao, S., Chen, M., Liu, Y., Fang, X., Lü, H., Zou, J., Liu, S., Qiao, S., 2012. Clay mineral composition and their sources for the fluvial sediments of Taiwanese rivers. Chinese Science Bulletin 57 (6), 673–681. https://doi.org/10.1007/s11434-011-4824-1.

Li, L., Switzer, A.D., Wang, Y., Weiss, R., Qiu, Q., Chan, C.-H., Tapponnier, P., 2015. What caused the mysterious eighteenth century tsunami that struck the Southwest Taiwan coast? Geophysical Research Letters 42 (20), 8498–8506. https://doi.org/10.1002/2015GL065567.

Lin, A.T., Liu, C.-S., Lin, C.-C., Schnurle, P., Chen, G.-Y., Liao, W.-Z, Teng, L.S., Chuang, H.-R., Wu, M.-S., 2008. Tectonic features associated with the overriding of an accretionary wedge on top of a rifted continental margin: an example from Taiwan. Marine Geology 255, 186–203. https://doi.org/10.1016/j.margeo.2008.10.002.

Lin, A.T., Yao, B., Hsu, S.-K., Liu, C.-S., Huang, C.-Y., 2009. Tectonic features of the incipient arc-continent collision zone of Taiwan: Implications for seismicity. Tectonophysics 479 (1–2), 28–42. https://doi.org/10.1016/j.tecto.2008.11.004.

Lin, C.-C., Lin, A.T.-S., Liu, C.-S., Horng, C.-S., Chen, G.-Y., Wang, Y., 2014. Canyon-infilling and gas hydrate occurrences in the frontal fold of the offshore accretionary wedge off southern Taiwan. Marine Geophysical Research 35 (1), 21–35. https://doi.org/10.1007/s11001-013-9203-7.

Liu, C.-S., Huang, I.L., Teng, L.S., 1997. Structural features off southwestern Taiwan. Marine Geology 137 (3–4), 305–319. https://doi.org/10.1016/S0025-3227(96)00093-x.

Liu, C.-S., Deffontaines, B., Lu, C.-Y., Lallemand, S., 2004. Deformation patterns of an accretionary wedge in the transition zone from subduction to collision offshore Southwestern Taiwan. Marine Geophysical Researches 25 (1–2), 123–137. https://doi.org/10.1007/s11001-005-0738-0.

McHugh, C., Seeber, L., Cormier, M., Dutton, J., Çağatay, N., Polonia, A., Ryan, W., Gorur, N., 2006. Submarine earthquake geology along the North Anatolia Fault in the Marmara Sea, Turkey: a model for transform basin sedimentation. Earth and

Planetary Science Letters 248 (3–4), 661–684. https://doi.org/10.1016/j.epsl.2006.05.038.
McHugh, C.M., Kanamatsu, T., Seeber, L., Bopp, R., Cormier, M.-H., Usami, K., 2016. Remobilization of surficial slope sediment triggered by the A.D. 2011 M w 9 Tohoku-Oki earthquake and tsunami along the Japan Trench. Geology 44 (5), 391–394. https://doi.org/10.1130/G37650.1.
McHugh, C.M., Seeber, L., Braudy, N., Cormier, M.-H., Davis, M.B., Diebold, J.B., Dieudonne, N., Douilly, R., Gulick, S.P.S., Hornbach, M.J., Johnson, H.E., Mishkin, K.R., Sorlien, C.C., Steckler, M.S., Symithe, S.J., Templeton, J., 2011. Offshore sedimentary effects of the 12 January 2010 Haiti earthquake. Geology 39 (8), 723–726. https://doi.org/10.1130/G31815.1.
McHugh, C.M., Seeber, L., Rasbury, T., Strasser, M., Kioka, A., Kanamatsu, T., Ikehara, K., Usami, K., 2020. Isotopic and sedimentary signature of megathrust ruptures along the Japan subduction margin. Marine Geology 428, 106283. https://doi.org/10.1016/j.margeo.2020.106283.
Middleton, G.V., 1993. Sediment deposition from turbidity currents. Annual Review of Earth and Planetary Sciences 21 (1), 89–114. https://doi.org/10.1146/annurev.ea.21.050193.000513.
Milliman, J.D., Syvitski, J.P.M., 1992. Geomorphic/Tectonic control of sediment discharge to the ocean: the Importance of small mountainous rivers. The Journal of Geology 100 (5), 525–544. https://doi.org/10.1086/629606.
Moernaut, J., van Daele, M., Strasser, M., Clare, M.A., Heirman, K., Viel, M., Cardenas, J., Kilian, R., Ladrón de Guevara, B., Pino, M., Urrutia, R., de Batist, M., 2017. Lacustrine turbidites produced by surficial slope sediment remobilization: a mechanism for continuous and sensitive turbidite paleoseismic records. Marine Geology 384, 159–176. https://doi.org/10.1016/j.margeo.2015.10.009.
Molenaar, A., Moernaut, J., Wiemer, G., Dubois, N., Strasser, M., 2019. Earthquake impact on active margins: Tracing surficial remobilization and seismic strengthening in a slope sedimentary sequence. Geophysical Research Letters 46 (11), 6015–6023. https://doi.org/10.1029/2019GL082350.
Moore, G.F., Bangs, N.L., Taira, A., Kuramoto, S., Pangborn, E., Tobin, H.J., 2007. Three-Dimensional splay fault geometry and implications for tsunami generation. Science 318 (5853), 1128–1131. https://doi.org/10.1126/science.1147195.
Moran, S., 2018. Fluid mechanics. In: An Applied Guide to Water and Effluent Treatment Plant Design. Elsevier, pp. 53–58. https://doi.org/10.1016/B978-0-12-811309-7.00005-9.
Mulder, T., Syvitski, J.P.M., 1995. Turbidity currents generated at river mouths during exceptional discharges to the world oceans. The Journal of Geology 103 (3), 285–299. https://doi.org/10.1086/629747.
Mulder, T., Migeon, S., Savoye, B., Faugeres, J.-C., 2001. Inversely graded turbidite sequences in the deep Mediterranean: a record of deposits from flood-generated turbidity currents? Geo-Marine Letters 21 (2), 86–93. https://doi.org/10.1007/s003670100071.
Ng, S.M., Angelier, J., Chang, C.-P., 2009. Earthquake cycle in Western Taiwan: Insights from historical seismicity. Geophysical Journal International 178 (2), 753–774. https://doi.org/10.1111/j.1365-246X.2009.04164.x.
Noguchi, T., Tanikawa, W., Hirose, T., Lin, W., Kawagucci, S., Yoshida-Takashima, Y., Honda, M.C., Takai, K., Kitazato, H., Okamura, K., 2012. Dynamic process of turbidity generation triggered by the 2011 Tohoku-Oki earthquake. Geochemistry, Geophysics, Geosystems 13 (11). https://doi.org/10.1029/2012GC004360.
Oguri, K., Kawamura, K., Sakaguchi, A., Toyofuku, T., Kasaya, T., Murayama, M., Fujikura, K., Glud, R.N., Kitazato, H., 2013. Hadal disturbance in the Japan Trench induced by the 2011 Tohoku–Oki Earthquake. Scientific Reports 3 (1), 1915. https://doi.org/10.1038/srep01915.
Okutsu, N., Ashi, J., Yamaguchi, A., Irino, T., Ikehara, K., Kanamatsu, T., Suganuma, Y., Murayama, M., 2019. Evidence for surface sediment remobilization by earthquakes in the Nankai forearc region from sedimentary records. Geological Society, London, Special Publications 477 (1), 37–45. https://doi.org/10.1144/SP477.22.
Park, J.-O., Tsuru, T., Kodaira, S., Cummins, P.R., Kaneda, Y., 2002. Splay fault branching along the Nankai subduction zone. Science 297 (5584), 1157–1160. https://doi.org/10.1126/science.1074111.
Polonia, A., Bonatti, E., Camerlenghi, A., Lucchi, R.G., Panieri, G., Gasperini, L., 2013. Mediterranean megaturbidite triggered by the AD 365 Crete earthquake and tsunami. Scientific Reports 3 (1), 1285. https://doi.org/10.1038/srep01285.
Polonia, A., Vaiani, S.C., de Lange, G.J., 2016. Did the A.D. 365 Crete earthquake/tsunami trigger synchronous giant turbidity currents in the Mediterranean Sea? Geology 44 (3), 191–194. https://doi.org/10.1130/G37486.1.
Polonia, A., Nelson, C.H., Romano, S., Vaiani, S.C., Colizza, E., Gasparotto, G., Gasperini, L., 2017. A depositional model for seismo-turbidites in confined basins based on Ionian Sea deposits. Marine Geology 384, 177–198. https://doi.org/10.1016/j.margeo.2016.05.010.
Polonia, A., Nelson, C.H., Vaiani, S.C., Colizza, E., Gasparotto, G., Giorgetti, G., Bonetti, C., Gasperini, L., 2022. Recognizing megatsunamis in Mediterranean deep sea sediments based on the massive deposits of the 365 CE Crete event. Scientific Reports 12 (1), 5253. https://doi.org/10.1038/s41598-022-09058-3.
Queano, K.L., Ali, J.R., Milsom, J., Aitchison, J.C., Pubellier, M., 2007. North Luzon and the Philippine sea plate motion model: Insights following paleomagnetic, structural, and age-dating investigations. Journal of Geophysical Research 112 (B5), 1–44. https://doi.org/10.1029/2006JB004506.
Ranken, B., Cardwell, R.K., Karig, D.E., 1984. Kinematics of the Philippine sea plate. Tectonics 35, 555–575. https://doi.org/10.1029/TC003i005p00555.
Rebesco, M., Vedova, B.D., Cernobori, L., Aloisi, G., 2000. Acoustic facies of Holocene megaturbidites in the Eastern Mediterranean. Sedimentary Geology 135 (1–4), 65–74. https://doi.org/10.1016/S0037-0738(00)00063-4.
Reynolds, P.D., 2002. The scaphopoda. Advances in Marine Biology 42, 137–236. https://doi.org/10.1016/S0065-2881(02)42014-7.
San Pedro, L., Babonneau, N., Gutscher, M.-A., Cattaneo, A., 2017. Origin and chronology of the augias deposit in the Ionian Sea (Central Mediterranean Sea), based on new regional sedimentological data. Marine Geology 384, 199–213. https://doi.org/10.1016/j.margeo.2016.05.005.
Schwestermann, T., Huang, J., Konzett, J., Kioka, A., Wefer, G., Ikehara, K., Moernaut, J., Eglinton, T.I., Strasser, M., 2020. Multivariate Statistical and Multiproxy Constraints on Earthquake-Triggered Sediment Remobilization Processes in the Central Japan Trench. Geochemistry, Geophysics, Geosystems 21 (6). https://doi.org/10.1029/2019GC008861.
Schwestermann, T., Eglinton, T.I., Haghipour, N., McNichol, A.P., Ikehara, K., Strasser, M., 2021. Event-dominated transport, provenance, and burial of organic carbon in the Japan Trench. Earth and Planetary Science Letters 563, 116870. https://doi.org/10.1016/j.epsl.2021.116870.
Seno, T., Stein, S., Gripp, A.E., 1993. A model for the motion of the Philippine sea plate consistent with NUVEL-1 and geological data. Journal of Geophysical Research: Solid Earth 98 (B10), 17941–17948. https://doi.org/10.1029/93JB00782.
Shanmugam, G., 1997. The Bouma Sequence and the turbidite mind set. Earth-Science Reviews 42 (4), 201–229. https://doi.org/10.1016/S0012-8252(97)81858-2.
Shiki, T., Cita, M.B., 2008. Tsunami-related sedimentary properties of Mediterranean homogenites as an example of deep-sea tsunamiite. In: Tsunamiites. Elsevier, pp. 203–215. https://doi.org/10.1016/B978-0-444-51552-0.00013-8.
Smillie, Z., Stow, D., Esentia, I., 2019. Deep-sea contourites drifts, erosional features and bedforms. In: Encyclopedia of Ocean Sciences. Elsevier, pp. 97–110. https://doi.org/10.1016/B978-0-12-409548-9.11590-8.
Sparkes, R.B., Lin, I.-T., Hovius, N., Galy, A., Liu, J.T., Xu, X., Yang, R., 2015. Redistribution of multi-phase particulate organic carbon in a marine shelf and canyon system during an exceptional river flood: Effects of Typhoon Morakot on the Gaoping river–canyon system. Marine Geology 363, 191–201. https://doi.org/10.1016/j.margeo.2015.02.013.
Stanley, D.J., 1981. Unifites: structureless muds of gravity-flow origin in Mediterranean basins. Geo-Marine Letters 1 (2), 77–83. https://doi.org/10.1007/BF02463322.
St-Onge, G., Chapron, E., Mulsow, S., Salas, M., Viel, M., Debret, M., Foucher, A., Mulder, T., Winiarski, T., Desmet, M., Costa, P.J.M., Ghaleb, B., Jaouen, A., Locat, J., 2012. Comparison of earthquake-triggered turbidites from the Saguenay (Eastern Canada) and Reloncavi (Chilean margin) Fjords: Implications for paleoseismicity and sedimentology. Sedimentary Geology 243–244, 89–107. https://doi.org/10.1016/j.sedgeo.2011.11.003.
Stow, D., Smillie, Z., 2020. Distinguishing between deep-water sediment facies: Turbidites. Contourites and Hemipelagites. Geosciences 10 (2), 68. https://doi.org/10.3390/geosciences10020068.
Stow, D., Faugères, J.-C., Howe, J.A., Pudsey, C.J., Viana, A.R., 2002. Bottom currents, contourites and deep-sea sediment drifts: current state-of-the-art. Geological Society, London, Memoirs 22 (1), 7–20. https://doi.org/10.1144/GSL.MEM.2002.022.01.02.
Strasser, M., Ikehara, K., Pizer, C., Itaki, T., Satoguchi, Y., Kioka, A., McHugh, C., Proust, J.-N., Sawyer, D., Everest, J., Maeda, L., Hochmuth, K., Grant, H., Stewart, M., Okutsu, N., Sakurai, N., Yokoyama, T., Bao, R., Bellanova, P., Zellers, S. D., 2024. Japan Trench event stratigraphy: first results from IODP giant piston coring in a deep-sea trench to advance subduction zone paleoseismology. Marine Geology 477, 107387. https://doi.org/10.1016/j.margeo.2024.107387.
Stuiver, M., Reimer, P.J., 1993. CALIB rev. 8. Radiocarbon 35, 215–230. https://doi.org/10.1017/S0033822200013904.
Su, C.-C., Hsu, S.-T., Hsu, H.-H., Lin, J.-Y., Dong, J.-J., 2018. Sedimentological characteristics and seafloor failure offshore SW Taiwan. Terrestrial, Atmospheric and Oceanic Sciences 29, 65–76. https://doi.org/10.3319/TAO.2017.06.21.01.
Tripsanas, E.K., Bryant, W.R., Phaneuf, B.A., 2004. Depositional processes of uniform mud deposits (unifites), Hedberg Basin, Northwest Gulf of Mexico: New perspectives. AAPG Bulletin 88 (6), 825–840. https://doi.org/10.1306/01260403104.
Usami, K., Ikehara, K., Kanamatsu, T., McHugh, C.M., 2018. Supercycle in great earthquake recurrence along the Japan Trench over the last 4000 years. Geoscience Letters 5 (1), 11. https://doi.org/10.1186/s40562-018-0110-2.
Wetzel, A., Werner, F., Stow, D., 2008. Bioturbation and Biogenic Sedimentary Structures in Contourites. In Contourites (pp. 183–202). Developments in Sedimentology. https://doi.org/10.1016/S0070-4571(08)10011-5.
Yakupoğlu, N., Henry, P., Uçarkuş, G., Eriş, K.K., Demory, F., Crouzet, C., Çağatay, M.N., 2022. Factors affecting thickness and frequency of turbidites triggered by earthquakes in Kumburgaz Basin. Sea of Marmara. Marine Geology 452, 106900. https://doi.org/10.1016/j.margeo.2022.106900.
Yang, R.J., Wang, S.-L., Burr, G.S., Liu, J.T., Fan, D., 2019. Holocene variation of radiocarbon reservoir age offshore western Taiwan, derived from paired charcoals and mollusks. Quaternary International 527, 79–86. https://doi.org/10.1016/j.quaint.2018.07.001.
Yu, K., Hua, Q., Zhao, J., Hodge, E., Fink, D., Barbetti, M., 2010. Holocene marine 14 C reservoir age variability: evidence from 230 Th-dated corals in the South China Sea. Paleoceanography 25 (3), 1–15. https://doi.org/10.1029/2009PA001831.
Yu, N.-T., Lu, C.-H., Yen, I.-C., Chen, J.-H., Yen, J.-Y., Chyi, S.-J., 2023. Boulder transport and wave height of a seventeenth century South China Sea tsunami on Penghu Islands. Taiwan. Natural Hazards Earth System Sciences 23, 3525–3542. https://doi.org/10.5194/nhess-23-3525-2023.

Yu, S.-B., Kuo, L.-C., 2001. Present-day crustal motion along the Longitudinal Valley Fault, eastern Taiwan. Tectonophysics 333, 199–217. https://doi.org/10.1016/S0040-1951(00)00275-4.

Yu, S.-B., Kuo, L.-C., Punongbayan, R.S., Ramos, E.G., 1999. GPS observation of crustal deformation in the Taiwan-Luzon Region. Geophysical Research Letters 26, 923–926. https://doi.org/10.1029/1999GL900148.

Yumul, G.P., Dimalanta, C.B., Tamayo, R.A., Maury, R.C., 2003. Collision, subduction and accretion events in the Philippines: a synthesis. Island Arc 12 (2), 77–91. https://doi.org/10.1046/j.1440-1738.2003.00382.x.